

1 **Exploring the influence of land use on the urban carbonyl sulfide budget: a case study of the**

2 **Metropolitan Area of Barcelona**

3 **Carme Estruch<sup>1,2</sup>, Sauveur Belviso<sup>3</sup>, Alba Badia<sup>1</sup>, Veronica Vidal<sup>1,4</sup>, Roger Curcoll<sup>1,5</sup>, Mireia**  
4 **Udina<sup>6</sup>, Claudia Grossi<sup>5</sup>, Josep-Anton Morguí<sup>1,7</sup>, Ricard Segura<sup>1</sup>, Sergi Ventura<sup>1</sup>, Yolanda Sola<sup>6</sup>,**  
5 **Gara Villalba<sup>1,8\*</sup>.**

6 <sup>1</sup>Institut de Ciència i Tecnologia Ambientals (ICTA), Universitat Autònoma de Barcelona, 08193  
7 Cerdanyola del Vallès, Barcelona, Spain.

8 <sup>2</sup> Eurecat, Centre Tecnològic de Catalunya, Climate Change Research Department, Amposta,  
9 Spain.

10 <sup>3</sup>Laboratoire des Sciences du Climat et de l'Environnement, LSCE, Paris-Saclay, France.

11 <sup>4</sup>Department of Computer Architecture and Operative Systems, Universitat Autònoma de  
12 Barcelona (UAB), Spain.

13 <sup>5</sup>Institute of Energy Techniques, Universitat Politècnica de Catalunya, Av. Diagonal 647, 08028,  
14 Barcelona, Spain.

15 <sup>6</sup>Departament de Física Aplicada–Meteorologia, Universitat de Barcelona, Barcelona, Spain.

16 <sup>7</sup>Departament de Biologia Evolutiva, Ecologia i Ciències Ambientals, Universitat de Barcelona,  
17 Barcelona, Spain.

18 <sup>8</sup>Department of Chemical, Biological and Environmental Engineering, Universitat Autònoma de  
19 Barcelona (UAB), Spain.

20

21 **Abstract**

22 Carbonyl sulfide (OCS) is used to quantify the carbon capture potential of the biosphere  
23 because of its direct correlation with CO<sub>2</sub> uptake during photosynthesis. However, to constrain  
24 the urban biosphere signal, it is necessary to evaluate potential anthropogenic sources. We  
25 conducted two sampling campaigns in the Metropolitan Area of Barcelona (AMB), Spain,  
26 during May (full COVID lockdown) and October 2020 to measure the spatial distribution and  
27 variability of OCS in four urban land uses as follows: built, urban forest, urban park, and peri-  
28 urban agriculture. The OCS background levels determined at Tibidabo (442 m asl) were  
29 approximately 484 ±20 ppt and 407 ±8 ppt for May and October 2020, respectively, and

30 agreed with other seasonal surveys conducted in Europe during that same period. The urban  
31 values ranged from neutral to above background, suggesting nearby anthropogenic and  
32 marine emissions such as  $+\Delta 150$  ppt in Montjuic, which is downwind of Barcelona's harbor.  
33 During the crop-growing season in May, the agricultural areas consistently showed values  
34 below the background (uptake) at 7:00 UTC when the land breezes were dominant, while later  
35 in the morning, when the sea breeze are developed, the plant sink is masked by the transport  
36 of marine emissions. Urban forests located north of Tibidabo showed OCS values up to  $-\Delta 70$   
37 ppt, suggesting significant uptake by urban forests. We conclude that determining the urban  
38 biosphere signal using OCS as a tracer is more complex than expected because the marine and  
39 anthropogenic emissions from the port strongly impact the spatial-temporal distribution of  
40 OCS.

#### 41 **Introduction**

42 Carbonyl sulfide (hereafter OCS) is an atmospheric trace gas used to study the  $\text{CO}_2$   
43 sequestration capacity of vegetation (Remaud et al., 2023 and references therein; Whelan et  
44 al., 2018 and references therein) because it is destroyed through photosynthesis in the same  
45 way as  $\text{CO}_2$  without producing any emissions through respiration (Protoschill-Krebs and  
46 Kesselmeier, 1992). According to the latest estimations, terrestrial vegetation and soils takes  
47 up from 530 and 670  $\text{Gg S yr}^{-1}$  (Remaud et al., 2023 and references therein) the largest natural  
48 sink of atmospheric OCS. Surface oceans are the most important natural source of OCS  
49 contributing directly and indirectly, i.e., from the atmospheric oxidation of carbon disulfide  
50 and dimethylsulfide, between 270 and 320 (Remaud et al., 2023 and references therein). The  
51 global budget of OCS is partially balanced by anthropogenic emissions, which are estimated to  
52 be 400  $\text{Gg S yr}^{-1}$  (Remaud et al., 2023 and references therein). Terrestrial sinks and natural and  
53 anthropogenic sources are generally separated in space and time, and exhibit distinct seasonal

54 and spatial variations (Remaud et al., 2023). Hence, land use changes are expected to have a  
55 significant influence on the global budget of atmospheric OCS.

56 Although many studies have evaluated OCS budgets at regional and global scales, little is  
57 known about OCS sources and sinks at the urban scale. Understanding land use influence on  
58 the budget of atmospheric OCS at the urban scale is much more difficult to establish because  
59 sources and sinks can coexist over small distances. For example, Commane et al. (2013)  
60 indirectly assessed OCS sources along the highly urbanized coastline of California where they  
61 detected biogenic OCS emissions from wetlands in Sacramento Bay, anthropogenic emissions  
62 near a storage facility and refinery in the port of Los Angeles, and OCS loss during the daytime  
63 due to photosynthetic uptake in vegetated areas. Besis et al. (2021) also conducted a study  
64 that identified potential sources of OCS at the city level and observed the spatial heterogeneity  
65 influencing OCS mixing ratios of Thessaloniki, Greece, and identified three locations where OCS  
66 concentrations in inner-city areas were three times higher than those at the seafront and  
67 where the waste management system was a source of OCS. According to Zumkehr et al.  
68 (2018), anthropogenic emissions of OCS due to aluminum, residential and industrial coal,  $\text{TiO}_2$ ,  
69 solvents and tires in the Metropolitan Area of Barcelona contribute to 65% ( $178 \text{ Mg S yr}^{-1}$ ) of  
70 the total emissions in the Catalonia region ( $276 \text{ Mg S yr}^{-1}$ , see Fig. S1 in supporting  
71 information). However, a study by Belviso et al. (2023) demonstrated that the Zumkehr et al.  
72 (2018) inventory for France largely overestimated OCS anthropogenic emissions by  
73 approximately an order of magnitude. A previous study by the same group used direct  
74 measurements from a sampling tower and computed back trajectories with the FLEXPART  
75 transport model to find that the Paris suburban area was acting mainly as an OCS sink (Belviso  
76 et al., 2022). Another urban study of Innsbruck, Austria, measured the hourly exchange rates  
77 of OCS with an eddy covariance tower and showed that urban OCS emissions are significantly  
78 higher at noon during weekdays than during weekends, which suggests that road traffic could  
79 be a net source of OCS emissions.

80           The use of OCS as a photosynthesis tracer has recently received attention as a  
81 potential method to determine the contribution of the urban biosphere toward reducing the  
82 carbon footprint (Mallik et al., 2016; Villalba et al., 2021). Mallik et al. (2016) reported the first  
83 records of annual OCS mixing ratios over an Indian city, which were substantially higher than  
84 tropospheric values, and those values changed seasonally with an observed 86% drop in OCS in  
85 November when air masses changed from oceanic to continental. Villalba et al. (2021) also  
86 observed changes in OCS related to air masses coming from marine and continental sources.  
87 This work highlighted the difficulty of characterizing the biosphere signal when the input  
88 masses are continental due to the heterogeneity they present in OCS content compared to  
89 stable marine conditions.

90 This study aims to contribute to the understanding of the dynamics of OCS budgets in urban  
91 areas by exploring to what extent different urban land uses can have an impact on  
92 atmospheric OCS mixing ratios in terms of the particular urban climate, geography, and  
93 topography affecting the transport and mixing of OCS sources and sinks. Motivated by the  
94 present lack of in situ OCS continuous measurements to properly infer surface OCS (Remaud et  
95 al., 2022), we conducted an OCS measurement campaign in the Metropolitan Area of  
96 Barcelona (AMB). We selected four different land uses as sampling sites as follows: forest,  
97 agricultural land, urban parks and impervious areas with the intention of understanding the  
98 role of urban land use on the OCS budget in a coastal city where we would expect a mixing  
99 ratio gradient between the sea (where OCS is produced) and the land (OCS capture in  
100 vegetated areas). The selection of sampling areas was based on their potential as a sink of OCS  
101 based on photosynthetic rates (Campbell et al., 2017; Villalba et al., 2021; Yang et al., 2018) or  
102 a local source based on anthropogenic inventories (Lee and Brimblecombe, 2016; Yan et al.,  
103 2019; Zumkehr et al., 2018). The OCS sampling campaigns were funded and conducted within  
104 the project *Integrated System Analysis of Urban Vegetation and Agriculture* (URBAG), which  
105 was financed by the European Research Council with the overall aim of understanding the

106 influence of green infrastructures on the urban CO<sub>2</sub> budget. As a coastal city with intense sea  
107 breezes during the day, the AMB is an ideal case study to determine the contribution of the  
108 urban biosphere and other anthropogenic sources to the overall urban OCS budget. The  
109 campaigns were conducted during the spring and early autumn of 2020 and almost coincided  
110 with the OCS spring maximum and autumn minimum (Montzka et al., 2007). Furthermore, the  
111 May campaign took place during the full lockdown due to the COVID pandemic, which helped  
112 constrain the biosphere signal given the reduction in anthropogenic activities that are  
113 potential sources of OCS such as vehicle exhaust (Zumkehr et al., 2017). We analyzed the  
114 observed OCS concentrations in terms of land-use influence while understanding the role of  
115 local weather conditions, synoptic events, and the planetary boundary layer by using  
116 atmospheric transport models, climate observations and atmospheric tracers. More  
117 specifically, we attempted to answer the following specific questions: how significant is the  
118 variability of OCS mixing ratios in an urban ecosystem? What is the land-use influence on the  
119 urban OCS budget?

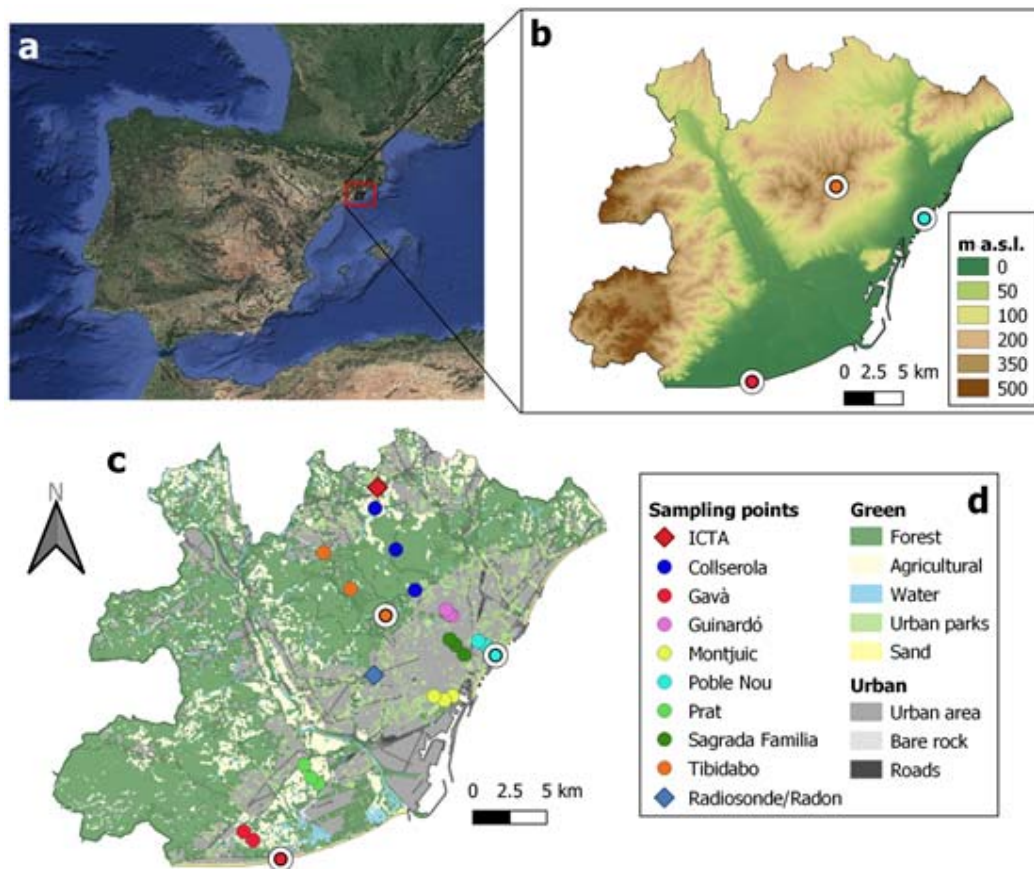
## 120 **1. Methods**

### 121 **2.1. Study site**

122 The two experimental campaigns took place in the Metropolitan Area of Barcelona (AMB),  
123 located in the NE corner of Spain, as shown in Fig. 1. The AMB, with a total surface area of  
124 approximately 640 km<sup>2</sup> and over 3.3 million inhabitants (16,160 people/km<sup>2</sup>), is the 7<sup>th</sup> largest  
125 urban area and 8<sup>th</sup> most densely populated region in the European Union. It is also one of the  
126 most industrialized areas in the western EU (Querol et al., 2004), specializing in food  
127 production, chemicals, vehicle manufacturing, and gas production and distribution (Institut  
128 d'Estadística de Catalunya, 2023). The AMB is bounded by the Besós River in the northeast, the  
129 Llobregat River in the west, the Collserola mountain range to the north, and the  
130 Mediterranean Sea to the south, as shown in Fig. 1. The AMB has a Mediterranean dry

131 subhumid climate with an annual precipitation of approximately 600 mm, which is mainly  
 132 concentrated during spring and autumn, and a mean annual temperature of 16.5 °C. The  
 133 orography of the city extends from sea level to 516 m above sea level (a.s.l.) at the mountain  
 134 range located northwest of the main urban areas.

135



136

137 **Fig. 1.** (a) A map of Spain showing the Metropolitan Area of Barcelona (AMB, red rectangle).  
 138 Orography of the AMB (b) and land use (c), where triplicates of colored dots represent the  
 139 upwind, target, and downwind sampling locations (d). Background atmospheric OCS levels  
 140 were investigated at the upwind sampling points at the sites of Tibidabo (highest altitude in  
 141 the PBL), Gavà and Poble Nou (closest to the shore). These sites are depicted with colored dots  
 142 with white circles in b and c. The red diamond represents the location of ICTA and the blue one  
 143 where the radiosondes were launched and the radon measurements were performed (c).

144 More than half of the AMB's surface area is covered by vegetation in various forms, including  
 145 urban forest (43%), agricultural fields (8%) and urban parks (4%), while 41% is covered by

146 impervious and other infrastructures (4%). Land uses are shaped by the following physical  
147 constraints: crops are located in the coastal plains formed by the delta of the Llobregat River,  
148 while urban forests composed of pine and holm oaks are located in the Collserola mountain  
149 range (Fig. 1). Urban green spaces are scattered throughout the metropolis and populated  
150 with ornamental species ranging from acacias to plantain trees and ornamental shrubs and  
151 grasses.

## 152 **2.2. Field campaigns**

153 Air samples were taken at the eight sites shown with colored dots in Fig. 1c, which were  
154 selected to represent the heterogeneity of land use throughout the AMB and are summarized  
155 into four land-use categories (see table 1): agricultural area (located in the Gavà and Prat  
156 areas), urban forest (Tibidabo and Collserola), urban green (Montjuic and Guinardó) and urban  
157 (Sagrada Familia and Poble Nou). We took air samples at each site (hereafter referred to as the  
158 target site) and upwind and downwind of each target site in an attempt to follow the air mass  
159 flow during its trajectory over the target site. The upwind and downwind sampling sites were  
160 determined based on historical wind patterns and trajectories typical of each target location  
161 under similar atmospheric conditions expected during the campaign and are available from the  
162 Meteorological Service of Catalonia ([www.meteo.cat](http://www.meteo.cat)) and shown in Appendix S1 of the  
163 supporting information. Note that in May and October 2020, observed wind patterns  
164 sometimes differed from historical data. The locations of the upwind, target, and downwind  
165 sites are shown for each point using the same color in Fig. 1c. The spatial distance among the  
166 three sampling points of each site ranges from 500 to 4,000 meters. Sampling times were  
167 chosen to capture inland winds during the early morning (i.e., 4:00 and 7:00 UTC am) and the  
168 typical sea breezes that develop during the morning and early afternoon (i.e., 9:30 and 11:00  
169 UTC am).

170 The first campaign took place between May 18<sup>th</sup> and May 28<sup>th</sup>, 2020, which was during a  
171 period of intense transport restrictions due to the COVID-19 pandemic, and resulted in highly  
172 significant air pollution reductions (Badia et al., 2021). Anthropogenic emissions drastically  
173 decreased, especially for the aviation (95%), road transport (up to 85%), and more moderately  
174 according to shipping (21%), public power % and industry (11%) sectors (Guevara et al., 2021).  
175 The second campaign took place from the 13<sup>th</sup> to the 27<sup>th</sup> of October 2020, when the  
176 anthropogenic activity returned to normal.

177 The temperature ranged from 20 °C to 24 °C during May and 14 °C to 20 °C during October.  
178 Samples were collected at 7:00 UTC and 9:30 UTC, and for some specific days, we performed  
179 additional sampling at 4:00 UTC and 11:00 UTC for the Tibidabo, Gavà and Poble Nou upwind  
180 locations to determine the background concentration of OCS. The weather was stable during  
181 both campaigns with one day of slight precipitation during each sampling campaign, which  
182 accumulated 2.6 and 1.6 mm during May 29 and October 26, respectively. The air mass  
183 influence was mostly cyclonic and advective with some days characterized by anticyclonic  
184 circulation. Synoptic winds were mostly north and east during the May campaign and  
185 predominantly southwest during October as summarized in Table S2 of the supporting  
186 information.

187 We recorded temperature, air pressure, wind direction and wind speed at each sampling site  
188 using a portable anemometer (Skywatch Xplorer 4). The relative humidity was obtained from  
189 the Meteorological Service of Catalonia for the first campaign (Servei Meteorològic de  
190 Catalunya, 2023), and additionally, it was registered on site using a digital hygrometer (TFA  
191 Dostmann®, precision ±4%) during the October campaign.

### 192 **1.3. OCS measurements and analysis**

193 Samples were collected in cylindrical borosilicate glass flasks (1 L volume, Normag Labor und  
194 Prozesstechnik GmbH, Germany) with Kel-F PCTFE valves fitted at both ends. This flask  
195 material showed the lowest permeation of gases compared to other sealing materials (Sturm  
196 et al., 2004). To ensure the quality of the measurement technique and repeatability of the  
197 experiment, two flasks connected to each other in a portable device were simultaneously filled  
198 in series (see Appendix S2, Urban sites, for device pictures). The inlet was installed at 3.5 m  
199 above ground level (m a.g.l.) and air, after passing through a magnesium perchlorate desiccant  
200 tube to remove moisture and a filter to remove particles, was pumped to the flasks with the  
201 help of a diaphragm pump (KNF N84.4 ANDC). Before taking the sample, air was flushed  
202 through the flasks for at least 10 min. At that time, we checked that the flow was steady and  
203 between  $2.0 \text{ L min}^{-1}$  and  $3.5 \text{ L min}^{-1}$ . After flushing, the exit valve was closed, and the flasks  
204 were pressurized with sample air to approximately 1.5 bar. Samples from the target, upwind  
205 and downwind sites were taken at the exact same moment to simulate an Eulerian  
206 approximation in which the sampling point remains fixed (Leelőssy et al., 2016).

207 Flasks were sent to the Laboratoire des Sciences du Climat et de l'Environnement, LSCE, Paris-  
208 Saclay, France, for OCS analyses. Flasks were stored for a maximum of 2 months before  
209 analysis. OCS was analyzed following the analytical method described in Belviso et al. (2016)  
210 and Belviso et al. (2022). In this procedure, atmospheric OCS (500 ml) is trapped using an  
211 automated sampling system (Entech P7100 preconcentrator) and then analyzed by gas  
212 chromatography with pulsed flame photometry detection (PFPD, Varian Model 3800, Belviso  
213 et al., 2016). Calibration was performed every week using a calibration gas supplied by Air  
214 Products (Belviso et al., 2016). The difference between the assigned value of an NOAA long-  
215 term air standard (NOAA-2004 scale) and the average of multiple analyses of that same  
216 standard was smaller than 1.5%. The drift between calibrations was assessed on a daily basis  
217 using a short-term target gas (Belviso et al., 2016).

#### 218 **1.4. Determining the planetary boundary layer height**

219 It is necessary to determine the planetary boundary layer height (PBLH) to understand its  
220 influence on the accumulation and dilution of OCS concentration at each site over the urban  
221 area. PBLH measurements were not possible at the eight target sites, but at least the PBLH was  
222 calculated from measurements taken on the campus of the University of Barcelona (Fig. 1,  
223 label: Radiosonde/Radon) using two different techniques as follows: (1) based on observed  
224 measurements from a radiosonde (RSD) station installed on the roof of the Physics  
225 Department of the University of Barcelona (41°23'03" N 2°07'01"E), which is part of the Global  
226 Meteorological Network (GCOS, 2016); and (2) via a laser ceilometer (CL-31, Vaisala Inc.,  
227 Finland) located at the same place with a measurement range up to 7.6 km, 10-m vertical  
228 resolution and a temporal resolution of 16 s. For the latter, the PBLH is estimated from the  
229 ceilometer data using the Vaisala Boundary-Layer View software (BL-VIEW) Enhanced Gradient  
230 method (VAISALA, 2020) – see details in Garcia-Dalmau et al. (2021) - followed by selection  
231 algorithms according to the methodology of Lotteraner et al. (2016).

232 To determine the PBLH based on radiosonde measurements, we followed a robust numerical  
233 procedure proposed by Liu and Liang (2010) using midday radiosonde (RSD) observations from  
234 the selected periods of study and considering 1100 UTC as the launching time. The PBLH was  
235 computed following the air parcel method for a convective dominated boundary layer  
236 (Holzworth, 1964; Seibert et al., 2000; Stull, 1988) as the height where air parcel evolution  
237 following a dry adiabatic evolution from surface intersects with the environment temperature  
238 profile. The calculated PBLH from RSD was visually corrected to solve the method errors and  
239 mostly related to the presence of several temperature inversion layers. A detailed explanation  
240 of the method and how we applied it to our case study is presented in the supplementary  
241 material (Appendix S3).

242 In this study, we also analyzed radon, which is a radioactive and noble gas known to be a good  
243 atmospheric tracer (Grossi et al., 2012), to better understand the evolution of the PBLH and to  
244 corroborate the PBLH calculated from the ceilometer observations using the method proposed  
245 by Griffiths et al. (2013). Hourly atmospheric concentrations of Rn were measured during  
246 October 2020 using an Atmospheric Radon MONitor (ARMON) at the Barcelona School of  
247 Industrial Engineering station (41°23'03" N 2°07'01"E, 10 m a.g.l) at the same site that  
248 radiosonde and ceilometer data were recorded and identified with the label  
249 Radiosonde/Radon in Fig. 1c. The monitoring was designed and built by the Universitat  
250 Politècnica de Catalunya as described by Grossi et al. (2012). Due to COVID-19 restrictions, no  
251 radon data were recorded for May 2020 because the equipment had to be shut down.

252 The estimations of PBLH using radiosonde and ceilometer were also compared with PBLH  
253 simulated using the Weather Research and Forecasting model (WRF). WRF simulations were  
254 performed to obtain information on the main transport processes and the vertical mixing  
255 conditions throughout the AMB as described in Section 2.6.

### 256 **1.5. WRF simulations of the urban atmosphere**

257 The WRF v4.3 model (Skamarock et al., 2021) coupled with the multilayer urban canopy  
258 scheme BEP-BEM (Salamanca et al., 2010) was used in this study to simulate the urban  
259 atmosphere over the AMB to better understand the influence of local weather conditions and  
260 PBL development on OCS concentrations. The WRF configuration used for this study consists of  
261 3 two-way nested domains with horizontal resolutions of 9 km, 3 km, and 1 km covering the  
262 Iberian Peninsula, the Catalan territory, and the AMB, respectively, with 45 vertical layers up to  
263 100 hPa (see Fig. S2 in Supporting information). The physics parameterization for the planetary  
264 boundary layer is the Boulac scheme, which has been shown to be the most suitable to resolve  
265 the turbulence intensity in convective situations for the AMB (Segura et al., 2021). We  
266 included 11 urban local climate zone (LCZ) classifications (Stewart and Oke, 2012) for the

267 innermost domain and each had a specific value for thermal, radiative and geometric  
268 parameters of the buildings and ground, which are used by the BEP-BEM to compute the heat  
269 and momentum fluxes in urban areas (Gilabert et al., 2021; Ribeiro et al., 2021; Yu and  
270 Steinberger, 2011). We conducted simulations for May and October 2020 using meteorological  
271 initial and boundary conditions from ERA5 (Copernicus, 2023). Table S3 in the supporting  
272 information further describes the model characteristics and experimental configurations. The  
273 model simulations were validated using temperature, wind speed and wind direction  
274 observations from 14 meteorological stations of the Meteocat network  
275 (<https://www.meteo.cat/observacions/xema>).

## 276 **1.6. FLEXPART back trajectories**

277 FLEXPART back trajectories were calculated to determine the precedence of air sampled at the  
278 various sites to establish whether the air mass influence was local or regional. FLEXPART  
279 (FLEXible PARTicle dispersion model) is a Lagrangian transport and dispersion model that is  
280 used for calculating the long-range and mesoscale dispersion of air pollutants (Stohl et al.,  
281 2005). The FLEXPART version adapted to the WRF mesoscale model (Brioude et al., 2013) was  
282 used to calculate back trajectories of air tracers from each of the sampling sites at the  
283 sampling times. The back trajectories were computed from the output of the WRF model at  
284 the nested domain of 1 km with 16 vertical levels from 0 to 2000 m a.g.l. Each back trajectory  
285 was calculated for 24 h after the sampling time. The number of particles released to the  
286 atmosphere in the simulation was 2000. From the 3D back trajectories, only the layers from 0  
287 to 100 meters above ground level were used for the study of footprints, as it is where the  
288 exchange among the land/ocean - atmosphere takes place.

## 289 **2. Results**

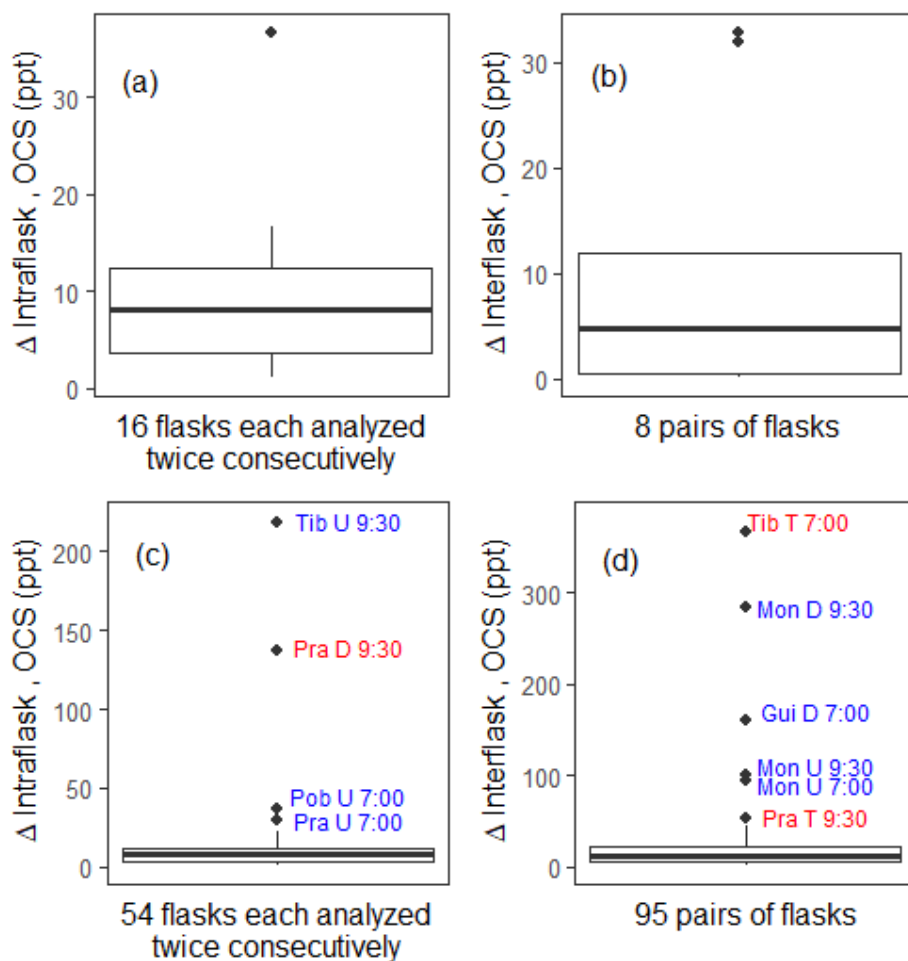
### 290 **3.1. OCS sample repeatability and accuracy in urban environments**

291 We performed a precision analysis of the GC measurements of flask-air samples according to  
292 the methods developed by Belviso et al. (2022) to assess the repeatability and accuracy of the  
293 OCS measurements in an urban environment. Eight pairs of flasks in total were selected  
294 randomly from the May and October campaigns, and each flask was analyzed twice  
295 consecutively for OCS. The average difference between duplicated measurements, i.e., the  
296 intraflask difference, was  $9.8 \pm 8.7$  ppt (median = 8.2 ppt, interquartile range (IQR) = 3.6–12.7  
297 ppt,  $n = 16$ , 90<sup>th</sup> percentile = 16.5 ppt, 6.3% of outliers), as shown in Fig. 2a. It was slightly  
298 higher than that reported by Belviso for samples collected in a rural area over wheat and  
299 rapeseed crops (Belviso et al. (2022), i.e.,  $9.3 \pm 7.2$  ppt (median = 7.5 ppt, interquartile range  
300 (IQR) = 4.5–12.5 ppt,  $n = 58$ , 5.2% of outliers, but in that case, the 90<sup>th</sup> percentile was 19.5  
301 ppt). Fig. 2c shows that among the 54 flasks (each analyzed twice consecutively), four  
302 displayed mixing ratios higher than the 90<sup>th</sup> percentile (i.e., 22.9 ppt), while the median and  
303 IQR of the intraflask difference (7.7 ppt and 3.3-12.1 ppt, respectively) appear to be highly  
304 consistent with the data displayed in Fig. 2a. Consistency is also found in terms of the  
305 proportion of aberrant determinations of OCS mixing ratios (i.e., 6.3% (Fig. 2a) and 7.4% (Fig.  
306 2c)). It was concluded that the precision for GC measurements of flask-air samples remained  
307 unchanged over the two campaigns and was consistent with that reported by Belviso et al.  
308 (2022).

309 The average difference between flasks of the same pair (i.e., the interflask difference) was also  
310 analyzed in a duplicate manner and was  $10.1 \pm 14.0$  ppt (median = 4.8 ppt, IQR = 0.05–18.6  
311 ppt,  $n = 8$ , no outlier, Fig. 2b). Hence, the interflask difference during the AMB study displayed  
312 higher variability than that of Belviso et al. (2022), i.e.,  $5.5 \pm 4.5$  ppt (median = 4.9 ppt, IQR =  
313 2.2–8.0 ppt,  $n = 29$ , a 6.9% proportion of outliers was reported in that study). The interflask  
314 difference was also assessed from a single analysis of the content of each flask. The median,  
315 IQR and 90<sup>th</sup> percentile were 12.1 ppt, 4.3-22.5 ppt and 45.0 ppt, respectively, with  $n = 95$  (Fig.  
316 2d). We reported the existence of six outliers (i.e., a proportion of 6.3%) exhibiting interflask

317 differences higher than 45.0 ppt and up to 360 ppt. The interflask difference calculated from  
318 pairs of flasks each analyzed only once for OCS (Fig. 2d) displays higher variability than that  
319 from pairs of flasks analyzed twice consecutively (Fig. 2b).

320 Consequently, although the four outliers displayed in Fig. 2c should have been discarded, we  
321 arbitrarily reincorporated those exhibiting intraflask differences in the range of 22.9 ppt (i.e.,  
322 the 90<sup>th</sup> percentile) and 36.8 ppt. According to Belviso et al. (2022), data from pairs of flasks  
323 exhibiting interflask differences higher than 14 ppt should be discarded. Note that this  
324 threshold is approximately twice that set by Montzka et al. (2007). Although the interflask  
325 difference calculated from pairs of flasks each analyzed only once for OCS could originate from  
326 aberrant data (Fig. 2d), nobody ever documented the high frequency distribution of OCS  
327 mixing ratios next to potential urban sources of that gas. In other words, although flasks are  
328 supposed to be simultaneously filled in pairs, the process of pressurization of two flasks  
329 connected in series could generate concentration gradients reflecting the heterogeneous  
330 distribution of OCS next to potential urban sources of that gas. In light of this possibility, we  
331 decided to arbitrarily validate the six outliers reported in Fig. 2d and investigate whether  
332 interflask differences higher than 45 ppt would be site dependent or would result from  
333 aberrant data.



334

335 **Fig. 2.** Analysis precision for OCS measurements from flask-air samples collected in the AMB  
 336 showing the 10th, 25th, median, 75th and 90th percentiles. (a, c) show  $\Delta$  interflask differences  
 337 in OCS concentration between two consecutive analyses of the content of each flask (median  
 338 of flask 1 minus that of flask 2), whereas (b, d) show the  $\Delta$  interflask differences in OCS  
 339 concentration between flasks of the same pair. The diamonds correspond to the outliers (>  
 340 90<sup>th</sup> percentile), which are over 23 ppt in Fig. 2c and over 45 ppt in Fig. 2d. Outliers are labeled  
 341 according to the location and time of sample collection. The codes of each sampling site are  
 342 site, location and time UTC (sites: Tib: Tibidabo, Pra: Prat, Pob: Poble Nou, Mon: Montjuic, Gui:  
 343 Guinardó; location: U: Upwind, D: Donwind, T: Target). Note that historical wind data was used  
 344 for that purpose. The label colors represent the campaigns and correspond to red for May and  
 345 blue for October.

### 346 **3.2. Evaluation of WRF simulations**

347 We ran WRF BEP-BEM simulations in May 2020 and October 2020 to obtain high-resolution  
348 meteorological data, atmospheric stability, and PBLH during the sampling periods. Statistical  
349 analyses of the root-mean-square error (RMSE), mean bias (MB) and correlation factor (R)  
350 were used to evaluate performances of the model compared with ground-based  
351 meteorological observations from Meteocat (see Section 2.6). The near-surface relative  
352 humidity (RH), temperature (T) and wind speed (WS) statistical analyses are displayed in Figs.  
353 S3 and S4 for campaigns in May and October, respectively. There is an overall good  
354 performance for the modeled RH, T and WS in comparison with the observations with an  
355 average error of  $\pm 14\%$  for RH,  $\pm 1.7$  to  $1.9$  °C for T and  $\pm 1.65$  ms<sup>-1</sup> for WS. This statistical  
356 analysis is available in the supporting information in Table S4.

357 During the May campaign, there were predominant northerly winds from the north from the  
358 18<sup>th</sup> until the 21<sup>st</sup>, and the circulation weather types were hybrid-cyclonic to cyclonic regimes,  
359 while the second half (25<sup>th</sup> through the 28<sup>th</sup>) was characterized by winds from the east with a  
360 Mediterranean Sea air mass influence and advective regimes, with the exception of the 28<sup>th</sup>,  
361 which was anticyclonic with a southeast synoptic wind component and local maritime air mass  
362 influence. During the October campaign, westerly and southerly winds characterized by  
363 advective circulation weather types prevailed for most of the period with a cyclonic north  
364 influence and regional continental air mass in the first two days switching to a maritime  
365 influence for the rest of the campaign. Table 1 summarizes these weather patterns for each  
366 day of the two campaigns.

367

368 Table 1. Circulation weather type (CWT), synoptic wind component (SWC) and PBLH extracted  
 369 from WRF simulations expressed in meters above ground level (a.g.l), averaged OCS  
 370 concentrations of all measurements taken each day during the May and October campaigns,  
 371 and expressed in ppt (mean values from the 3 sites, mean values  $\pm$  standard deviations). An  
 372 unabridged version of this table with upwind and downwind OCS including a detailed data for  
 373 background measurements concentrations (see figure 4) is available in S1 of the supporting  
 374 information.

Campaign	Site (elevation)	Land use type	Date	CWTs*	SWC**	PBLH range (m)	OCS 7:00 UTC (ppt)	OCS 9:30 UTC (ppt)
May 2020	Tibidabo (175-442 m)	Forest	19/05	C	N	19-441	478 $\pm$ 20	494 $\pm$ 9
	Gavà (0-2 m)	Agricultural	21/05	U	N	11-249	482.1 $\pm$ NA	495.5 $\pm$ 10.7
	Poble Nou (0-4 m)	Urban	21/05	U	N	44-2217	461 $\pm$ 20	NA
	Montjuic (42-98 m)	Urban green	20/05	C	N	327-883	485 $\pm$ 14	490 $\pm$ 5
	Prat (0-2 m)	Agricultural	25/05	E	E	737-1182	502 $\pm$ NA	508 $\pm$ 2
	Sagrada (37-55 m)	Urban	26/05	E	E	771-1900	460 $\pm$ 6	NA
	Collserola (107-442 m)	Forest	27/05	E	E	395-1079	441 $\pm$ 39	497 $\pm$ 3
	Guinardó (115-169 m)	Urban green	28/05	A	SE	590-1524	505 $\pm$ 8	612 $\pm$ 17
October 2020	Gavà (0-2 m)	Agricultural	23/10	U	NW	21-5019	401 $\pm$ 9	403 $\pm$ 3
	Poble Nou (0-4 m)	Urban	15/10	CN	N	287-571	405 $\pm$ 23	426 $\pm$ 45
	Guinardó (115-169 m)	Urban green	19/10	ASW	SW	69-934	389 $\pm$ 20	392 $\pm$ 16
	Sagrada (37-55 m)	Urban	20/10	SW	SW	29-1085	444 $\pm$ 19	460 $\pm$ 93
	Montjuic (42-98 m)	Urban green	21/10	CSW	SW	92-734	425 $\pm$ NA	485 $\pm$ 87
	Prat (0-2 m)	Agricultural	22/10	SW	SW	103-495	468 $\pm$ 24	490 $\pm$ 37

375 \*CWT: Circulation weather type. The different types of CWTs are cyclonic (C), anticyclonic (A), pure advective (N, S, E, W, NE, SE,  
 376 NW, SW), hybrid cyclone-advective (CN, CNE, CE, CSE, CS, CSW, CW, CNW), hybrid anticyclone-advective (AN, ANE, AE, ASE, AS,  
 377 ASW, AW, ANW), and undefined (U). \*\*SWC: Synoptic wind component summarizing the pressure pattern, fronts, wind direction  
 378 and speed.

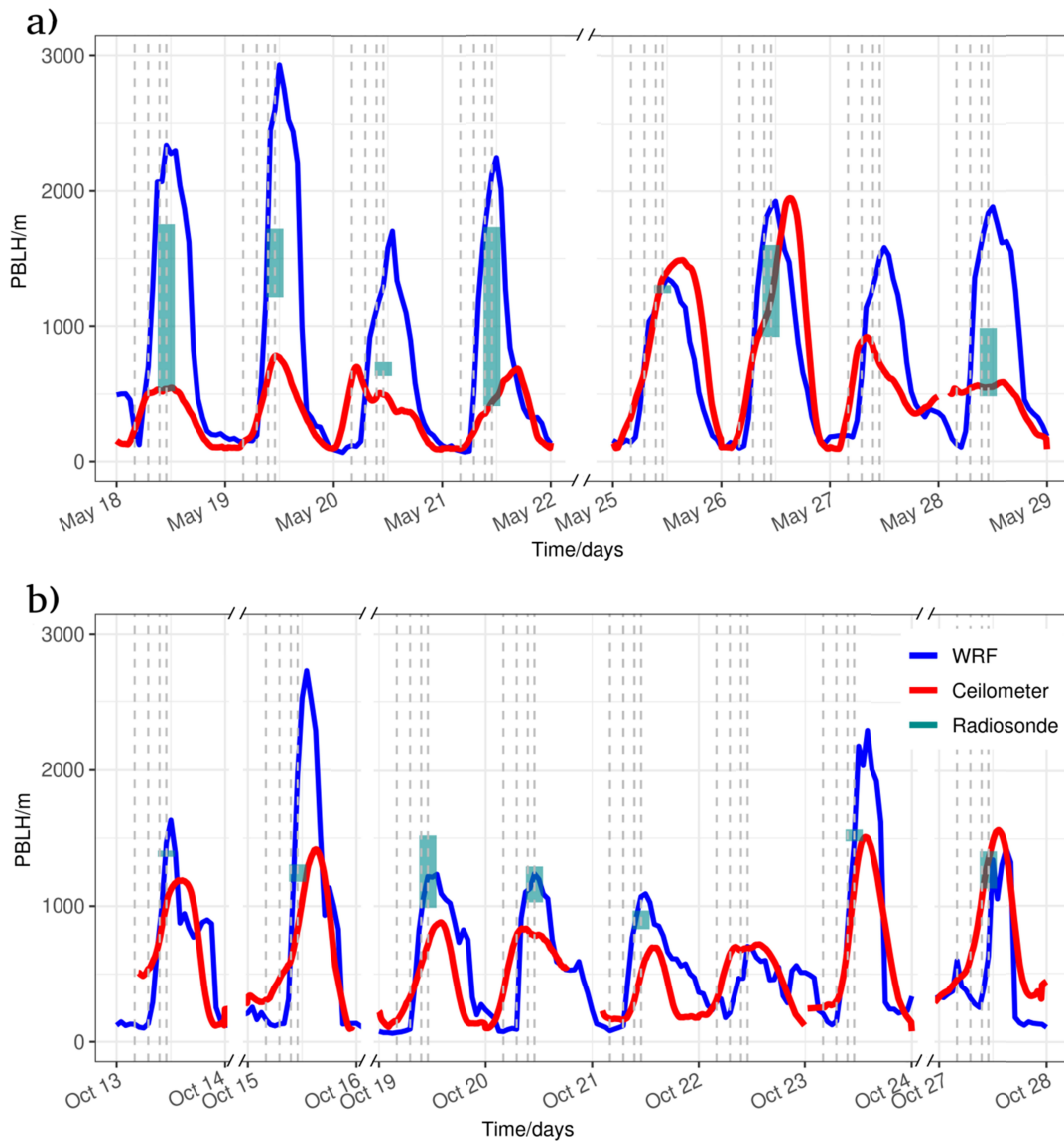
379

### 380 3.3 Planetary boundary layer height calculations and evaluation

381 The PBLH from the WRF BEP-BEM simulations was compared against ceilometer estimations  
 382 and radiosonde observations at 11:00 UTC for each day of the campaigns (see Fig. 3). All data

383 time series follow the expected PBLH diurnal pattern with a rapid growth of the PBLH during  
384 the morning, a maximum that was reached at midday, and a decrease during the afternoon.  
385 The PBLH calculated by the WRF model is generally higher than that estimated by the  
386 ceilometer and radiosonde. During the first period of May and first days of October when  
387 there are continental regional air masses with prevailing large-scale northern winds, we  
388 noticed an important difference between the ceilometer, radiosonde, and WRF values in some  
389 cases up to 150 m difference at 11 UTC. In this situation, the large-scale winds dominate the  
390 boundary-layer scales, which limit the capacity of the WRF model to estimate the PBLH and  
391 leads to high uncertainty in the radiosonde observations (Stull, 1988). The inverse correlation  
392 between atmospheric radon concentrations and the ceilometer-based PBLH is uniformly  
393 maintained during the entire October campaign as you can see in Fig. S5 how PBLH are at its  
394 maximum at 00:00 UTC while atmospheric radon concentration are at its lowest, and the  
395 opposite behavior is seen around 12:UTC (see Fig. S5 and Fig. S6 of the supporting  
396 information), which further indicates an overestimation of the PBLH by WRF during strong  
397 wind events in early October. The highest radon activity concentrations (between  $0.01 \text{ Bq m}^{-3}$   
398 and  $0.05 \text{ Bq m}^{-3}$ ) are observed during nighttime (21 h-2 h) when the PBLH reaches its  
399 minimum, whereas the lowest values (between  $1 \text{ Bq m}^{-3}$  and  $2 \text{ Bq m}^{-3}$ ) are observed during  
400 diurnal hours (11 h-16 h) when  $^{222}\text{Rn}$  is diluted due to a well-developed PBL.

401 The overestimated PBLH modeled values in May are consistent with an overprediction of the 2  
402 m temperature seen for a station located 1.2 km from the radiosonde launching location. In  
403 contrast, better agreement between the modeled and observed PBLH (both radiosonde and  
404 ceilometer) is seen during the second half of the May campaign from the 25<sup>th</sup> to 28<sup>th</sup> of May  
405 (Fig. 3a), when the easterly winds lead to a more stable atmosphere. October showed better  
406 agreement overall among the PBLH values obtained from the ceilometer, RSD and WRF model  
407 due to higher atmospheric stability. The south-easterly weak winds generally lead to stable  
408 conditions and local scale dominance where the PBLH can be well estimated.



410

414 **Fig. 3** The time series of modeled PBLH (blue line) together with the Ceilometer (red line) and  
 415 the Radiosonde (blue shade) for a) May and b) October campaigns. Shaded blue areas indicate  
 416 the PBLH using two different definitions for its calculation. Vertical lines correspond to the 4  
 417 am, 7 am, 9:30 am and 11 am UTC sampling times on a daily basis.

### 415 **3.4 WRF-FLEXPART footprints**

418 FLEXPART simulations showed that the sampling campaign covered different synoptic  
 419 situations and different air mass origins. Appendix S4 of the supporting information shows that  
 420 during the May campaign, two main directions were observed as follows: one coming from the

418 northwest following the Llobregat River basin (days 18, 19, and 21 of May) and another from  
419 the northeast with more sea influence (days 20 and 25 of May) and some others with more  
420 land influence (such as days 26, 27, and 28 of May). Generally, the simulation at 09:30 UTC  
421 shows more sea origin of the air masses arriving at sampling points than the simulations at  
422 07:00 UTC in accordance with the sea–land breeze regimes.

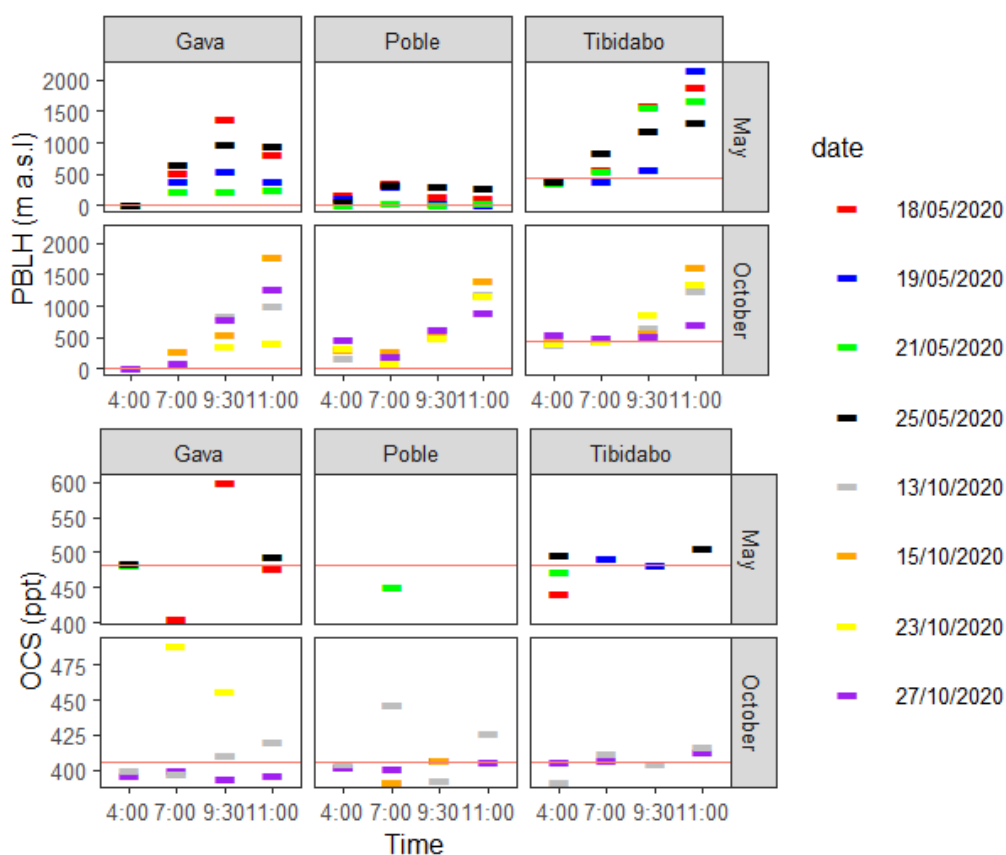
423 During the October campaign, the air masses mainly came from the northwest following the  
424 Llobregat River basin (days 15, 19, and 27 of October), although a situation with strong winds  
425 coming from the south was observed between the 20<sup>th</sup> and 21<sup>st</sup> of October. A stronger breeze  
426 regime is observed during this month with general changes in the origin of air masses between  
427 the simulations at 07:00 and 09:30 UTC.

### 428 **3.5. Background OCS measurement validation**

429 There were three potential background measurement locations (upwind sites of Gavà, Poble  
430 Nou and Tibidabo shown in Fig. 1), but only Tibidabo at 442 m a.s.l showed stability in OCS  
431 concentrations regardless of the diurnal convection patterns (Fig. 4a), which ranged from 443  
432 to 507 ppt during May and 392 to 416 ppt during October, as shown in Fig. 4b. The coastal  
433 sites showed less stable values with Gavà showing the highest variability ranging from 407 to  
434 600 ppt during May and 393 to 489 ppt in October, which are values well above the global  
435 background level. For example, on May 18<sup>th</sup>, a great variability in OCS mixing ratios was  
436 observed, and FLEXPART back trajectories simulated for Gavà showed significant changes in air  
437 mass precedence (see Appendix S4a: Gavà, May 18, 2020, at 7:00, 9:00, and 11:00 UTC). At  
438 7:00 UTC, we obtained the lowest OCS concentration value of the campaign (407 ppt) when air  
439 masses came from the inland north and collected air from forested areas; a few hours later at  
440 9:30 UTC, the concentration rose to 600 ppt because air transport switched to an influence  
441 from the northeast where the densest part of the AMB is located. Earlier and later that day, at  
442 4:00 and 11:00 UTC, OCS measurements were closer to typical background values, which

443 indicated the marine influence of sea breezes during those hours, which decreased residential  
 444 times over the urban area. Thus, we established Tibidabo mean values as a background  
 445 measurement with a mean value for OCS of 484 ppt in May and 407 ppt during October. Our  
 446 Tibidabo background values show congruence with those of the National Oceanic and  
 447 Atmospheric Administration (NOAA), which ranged from 478 to 498 ppt in May and 399 to 408  
 448 ppt in October (<https://gml.noaa.gov/hats/gases/OCS.html>).

449



450

451 **Fig. 4.** (a) PBLH from the WRF model of three potential background site measurements for the  
 452 AMB. The red line represents the current altitude for each site. (b) OCS concentrations of three  
 453 potential background measurements for the AMB. The red line represents the background  
 454 value chosen, which corresponds to the Tibidabo site with mixing ratios of 484 and 407 ppt for  
 455 the May and October campaigns, respectively. Detailed data for background measurements  
 456 concentrations is available in S1 of the supporting information.

457

458 Generally, OCS background concentrations were higher in May (484 ppt) than in October (407  
459 ppt), which reflects the global annual oscillation of maximum values in spring (mean north  
460 hemisphere 510 ppt for May) and lowest values in the fall (mean north hemisphere 440 ppt for  
461 October) reported by Montzka et al. (2007) for northern hemisphere Atlantic locations.

### 462 **3.6. OCS concentrations over the metropolitan landscape**

463 The OCS concentrations at each site for both campaigns are given in Table 1, which also  
464 provides the circulation weather type (CWT), the synoptic wind component (SW) and PBLH  
465 from the WRF model simulations. The full data set is available at the Zenodo repository  
466 (URBAG, 2023) as well as the supporting information table S1. The highest concentrations  
467 were recorded in May at the sampling sites of Guinardó and El Prat ( $612 \pm 17$  ppt and  $508 \pm 2$   
468 ppt) when winds were coming from the east, independently if mass air influence was local or  
469 regional, and well above ocean background values of 478 to 498 ppt estimated at the North  
470 Atlantic locations by NOAA (Fig. S7, <https://gml.noaa.gov/hats/gases/OCS.html>). High-  
471 pressure, anticyclonic conditions during that time suggest that the high OCS concentration  
472 values might be due to the accumulation of local OCS emissions.

473 The lowest OCS concentrations were recorded at Gavà and Collserola in May ( $407.1 \pm 8.5$  and  
474  $412.6 \pm 13.8$  ppt, respectively) and at Gavà, Guinardó, Sagrada Familia and Poble Nou in  
475 October ( $398.3 \pm 6.1$ ,  $374.1 \pm 8.6$ ,  $397.3 \pm 5.2$ , and  $390.4 \pm 15.7$ , respectively). There seems to be no  
476 clear pattern relating circulation weather typologies to OCS measurements. For example, the  
477 highest OCS mixing ratio during the October campaign was recorded in Montjuic at 7:00 UTC  
478 ( $485 \pm 87$  ppt) with hybrid cyclone-advective conditions that influenced the day and regional air  
479 mass with wind blowing from the southwest (Table 1). In October, we had a similar weather  
480 pattern, yet this location registered one of the lowest OCS concentrations ( $389 \pm 20$  ppt).  
481 However, Sagrada Familia also recorded the second lowest value ( $392 \pm 16$  ppt) in October with

482 maritime stable conditions on both days. For May, the lower record corresponds to Gavà at  
483 7:00 UTC ( $431 \pm 22$  ppt), which was a day with local continental atmospheric conditions.

#### 484 **4. Discussion**

##### 485 **4.1. Exploring the land-use influence on the OCS budget of the urban area.**

486 We found more variability among the OCS mixing ratios within the metropolitan area than  
487 between the two campaigns, which ranged from 450 to 600 ppt for May and from 390 to 470  
488 ppt for October. This indicates that local sources and sinks, the heterogeneity of the urban  
489 landscape, and local air transport in the AMB have a larger weight on the OCS urban budget  
490 than what other stations that monitor more homogenous areas, such as Gif-Sur-Yvette and  
491 Mace head, than within cities such as Utrecht (Fig. S7). We proceeded to analyze how each  
492 type of land use had an influence on OCS concentrations, considering other measured or  
493 modeled variables such as air transport regimes, PBLH development, and air mass influence.

494 **Urban parks:** Samples were measured from two urban parks located in very different urban  
495 environments in the AMB (see Fig. 1 for their locations and supporting information and  
496 Appendix S2 for pictures). Guinardó Park is located in the middle of Barcelona in one of the  
497 most densely populated areas, which is characterized by a high built fraction and surrounded  
498 by streets with heavy traffic. At 169 m a.s.l and a total area of 15.9 ha, Guinardó has dedicated  
499 spaces for recreational purposes and a wide number of ornamental trees including acacias,  
500 magnolias and other foreign species. However, Montjuic Park is close to the sea and overlooks  
501 the Port of Barcelona at 98 m a.s.l. with a total area of 227 ha. It is part of a highly vegetated  
502 recreational area on Montjuic Mountain with more than 690 species of identified plants  
503 including palm trees, acacias, pines, and a great variety of shrubby plants.

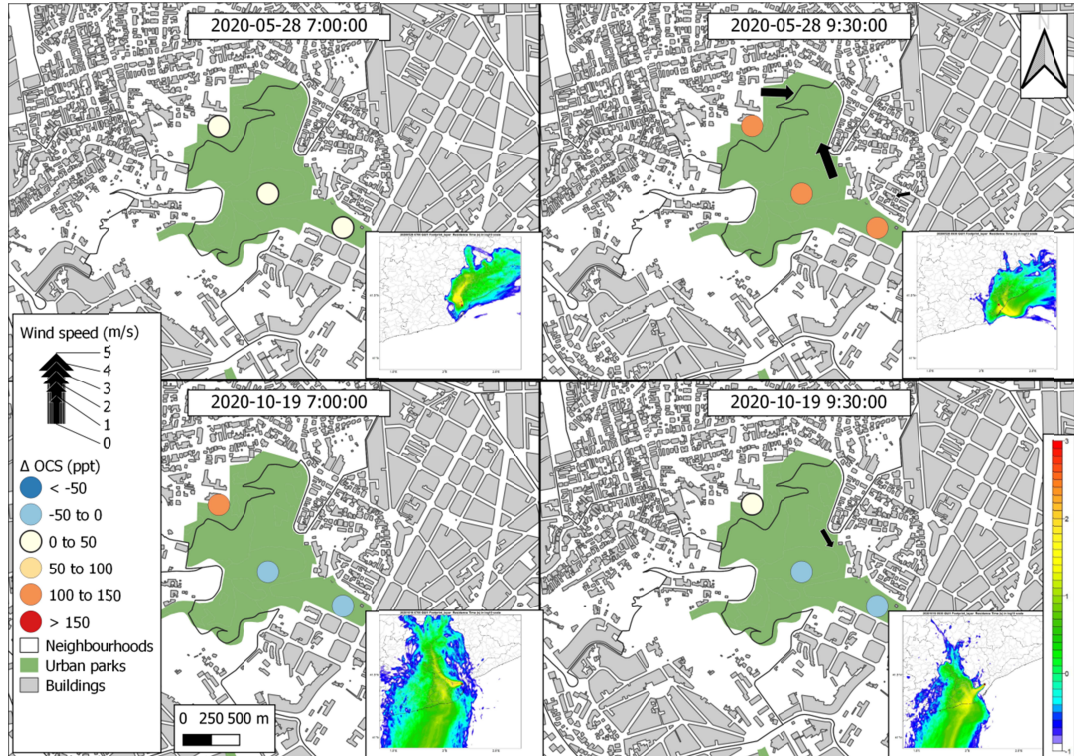
504 Guinardó was sampled on May 28<sup>TH</sup> at 7:00 and 9:30 UTC with little presence of local winds at  
505 that time. Fig. 5a shows the OCS enhancements ( $\Delta$  OCS) calculated as the measured OCS

506 concentration at each site minus the background concentration of 484 ppt established for the  
507 month of May (Table S1 in supporting information can be consulted for absolute values).  
508 Initially, at 7:00 UTC, OCS concentrations at downwind, target, and upwind, were +22, +28, and  
509 +11 ppt, respectively over the established background level of 484 for May showing little  
510 enhancement; however, at 9:30 UTC, we observed a significant  $\Delta$ OCS of +110, +128, +144 ppt,  
511 respectively. FLEXPART backward trajectories for these times (embedded in Fig. 5a and b,  
512 while a larger Fig. is provided in Appendix S4) estimate that the forthcoming air masses were  
513 mostly local with breezes changing from land (north-east) at 7:00 to sea (southeast) at 09:30  
514 UTC. This suggests local sources of OCS from both the sea and industrial activity of the port.  
515 Overall, it seems that the OCS capture capacity by the vegetation of Guinardó Park is offset by  
516 significant local sources that are perceptible when wind blows from SE (Locations affected by  
517 port, city and ship traffic), which increase OCS concentrations by +140 ppt despite a highly  
518 developed PBLH of 1,524 m at 9:30 UTC, which favors mixing and lower concentrations.

519 Samples taken on October 19<sup>th</sup> showed the opposite behavior as follows:  $\Delta$ OCS were -33, -4,  
520 and +113 ppt for the downwind, target, and upwind directions, respectively, at 7:00 and -15, -  
521 32, +2, ppt, respectively, at 9:30 UTC, as shown in the lower panel of Fig. 5a. This time, the  
522 FLEXPART backward trajectory indicates a regional air transport influence from the northwest  
523 at 7:00 UTC, which transports air masses from the agricultural Llobregat basin. At 9:30 UTC,  
524 winds switch to southwest collecting air with influences from croplands and the sea.  
525 Furthermore, local breezes were insignificant, and the PBLH did not develop very strongly  
526 between 7:00 and 9:30 am, going from 69 to 934 meters, which leads us to believe that the  
527 lower concentrations at both 7:00 and 9:30 are most likely attributable to vegetation uptake in  
528 the park and the influence of air mass transport from agricultural fields rather than mixing of  
529 air that is typical of a fully developed boundary layer.

532

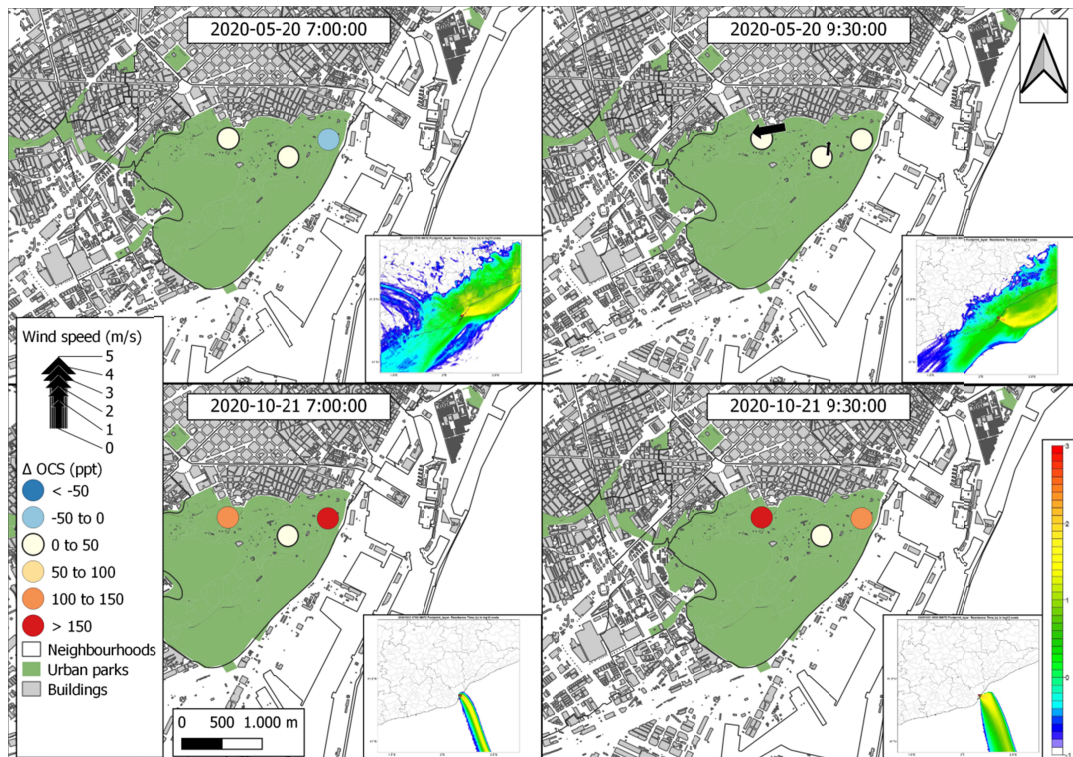
a) Guinardó



533

533

b) Montjuic



534

534 **Fig. 5.** OCS enhancement ( $\Delta$  OCS) in ppt calculated as measured OCS minus background OCS  
535 (484 ppt for May and 407 ppt for October) for each campaign at the two urban parks as  
536 follows: a) Guinardó and b) Montjuic. The black arrow shows the wind direction and speed  
537 measured on site, and the absence of an arrow indicates that there was no wind blowing at  
538 the moment of measurement. A small map embedded in the lower right-hand corner of each  
539 panel shows the residence time on a logarithmic scale of the air masses arriving at the  
540 sampling site as determined with the FLEXPART model.

541 Montjuic Park offers more information in terms of the OCS drawdown capacity of the  
542 vegetation because of its key location next to the Port of Barcelona, which is expected to be a  
543 source of OCS due to its natural gas supply activity and ships. As illustrated in Fig. 5b, there  
544 was very little difference between the 7:00 and 9:30 UTC OCS enhancements during May,  
545 which ranged from -12 to +17 ppt. The FLEXPART simulation for that day indicates a regional  
546 sea influence from eastern winds at 7:00 and 9:30 UTC that explains why all sites have OCS  
547 concentrations very close to background values at both times. There seems to be no significant  
548 source of OCS over the Montjuic area since the easterly winds are not influenced by the Port of  
549 Barcelona, which lies further south.

550 In contrast, during the October campaign, there was a strong southern regional influence on  
551 air masses over Montjuic Park as described by the FLEXPART trajectory. The air arrived from  
552 due south with no land influence, which, in addition to a low PBLH at 9:30 UTC of 561 meters,  
553 constrains any changes in the OCS budget over Montjuic Park to very local processes. Thus, the  
554 high OCS values of 665 and 635 ppt we see at 7:00 and 9:30 UTC for the upwind site and  
555 downwind site and reaching more than +150 ppt above background, are most likely a result of  
556 the industrial activity of the Port of Barcelona. This enhancement was consistently seen in all  
557 upwind and downwind samples at 7:00 and 9:30. At the target site, samples were consistently  
558 near background values with enhancements of only +16 and +18 ppt at 7:00 and 9:30 UTC,  
559 respectively. It is more difficult to determine the reasons for this decrease compared to the  
560 other two points; it could not receive the emission plume that reached the other two places  
561 and combined with an effect of the vegetation signal. The fact that the target is at double the

562 height of the upwind and downwind sites (98 m asl vs. 58 and 42 m asl) leads us to think that  
563 the signal from the plume with a high content of OCS did not arrive with the same intensity.  
564 The PBLH was 92 m at 7:00 UTC but 720 m at 9:30 UTC, which could only explain this  
565 difference in the early hours.

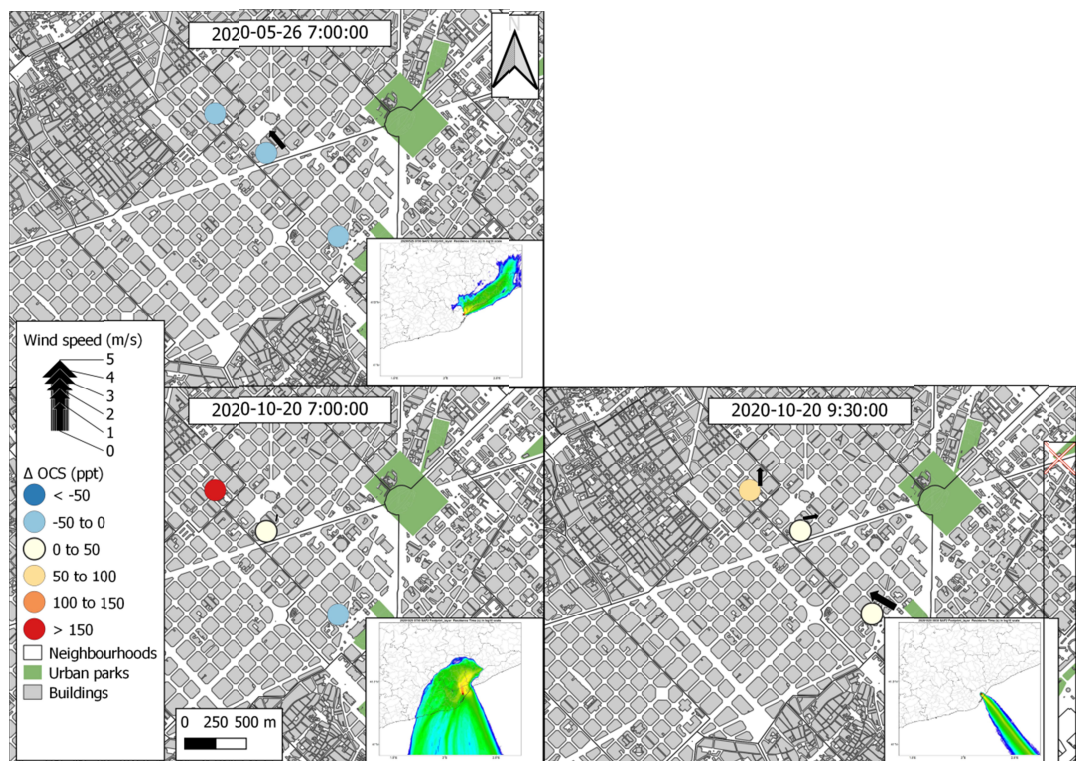
566 **Urban forest.** There were two sampling locations representing urban forests as follows:  
567 Tibidabo and Collserola. Both locations belong to the Collserolla range, which is a mountainous  
568 area with more than 8,000 ha located in the northern limit of the city with a maximum altitude  
569 of 512 m asl. The flora of the park is maritime Mediterranean and is dominated by white pine  
570 (*Pinus halepensis*) and low vegetation of maquis, scrub and meadows apart from cultivated  
571 fields. It has an estimated population of 10 billion trees and more than 1,000 species of plants.  
572 During the May campaign, OCS concentrations at 7:00 UTC ranged between 463 and 499 ppt  
573 and 412-498 ppt for Tibidabo and Collserola, respectively, which are all within the range of the  
574 assigned background concentration. There was one exception at the Tibidabo Target site at  
575 7:00, which had  $620 \pm 260.2$  ppt and was discarded as the outlier with the largest discrepancy  
576 between replicates (see Fig. 2). Enhancements were minimal with  $\Delta$ OCS of -16, -72 and -33 ppt  
577 for collserola, +7 and -21 ppt for Tibidabo at 7:00 UTC, +9, +14 and +15 ppt for Collserola, and -  
578 2, +15 and +15 ppt for Tibidabo at 9:30 UTC. We had local and regional air mass influences and  
579 marine to continental winds for Collserola and Tibidabo (see Fig. S8 and Table 1). Local winds  
580 at 7:00 UTC in Collserola suggested that the small OCS drawdown was due to the vegetation.  
581 The forest sites clearly showed a behavior from neutral to sink with respect to OCS exchange  
582 fluxes. Having established this tendency, we limited the sampling to the background location  
583 (Tibidabo upwind) during the October campaign.

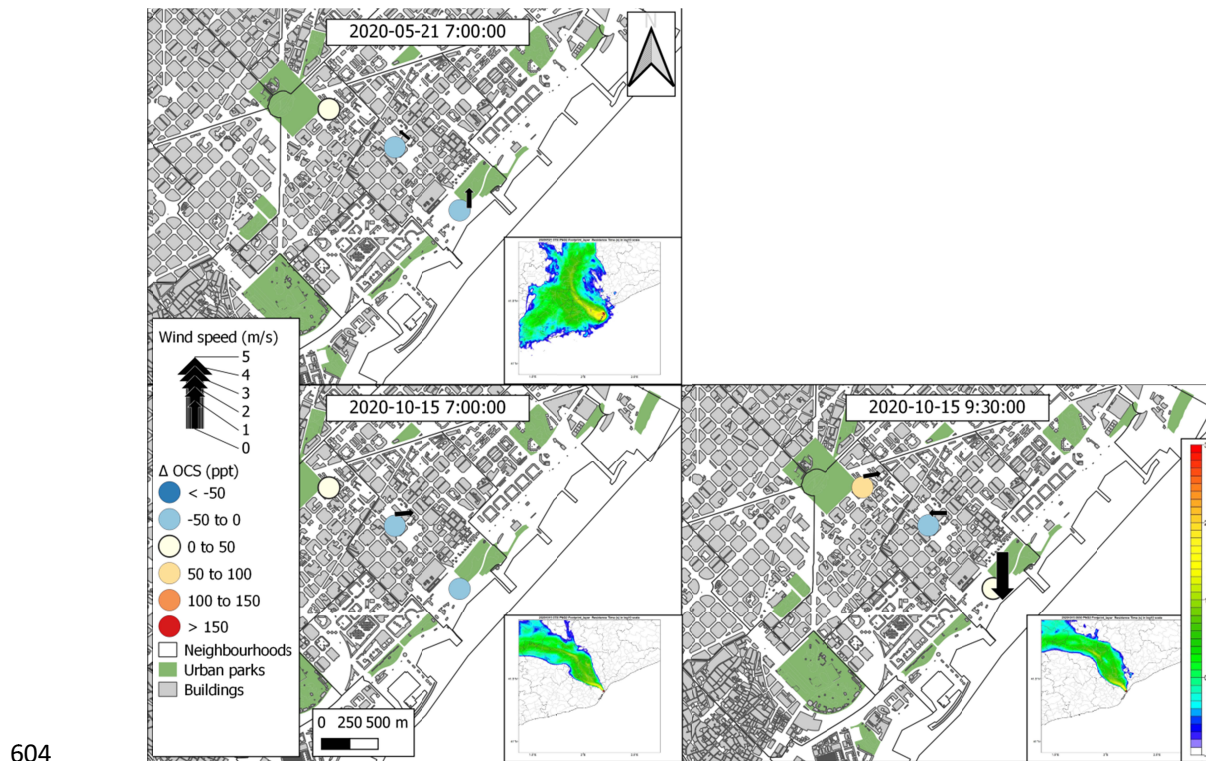
584 **Urban:** OCS concentrations in May were surprisingly lower than our background estimate for  
585 both of our urban locations of Sagrada Familia and Poble Nou, which are characterized by  
586 100% built environments of buildings, streets, constant traffic and little or no vegetation (see

599 Fig. 1 for their locations and supporting information and Appendix S2 for pictures). The OCS  
500 enhancements ranged between -17 to -29 ppt and 0 to -36 ppt for Sagrada Familia and Poble  
501 Nou, respectively, at 7:00 UTC, as shown in the upper panels of Fig. 6 (9:30 UTC samples were  
502 not possible because of complications with the logistics during the campaign). Given the low  
503 mixing potential of the relatively low PBLH for both the Poble Nou and Sagrada Familia (100  
504 and 800 m, respectively), we can conclude that there were no local OCS sources. One likely  
505 reason for this is that there was little or no traffic during this time due to the COVID lockdown  
506 and mobility restrictions. The FLEXPART trajectory for Sagrada Familia shows an influence of  
507 easterly winds bringing air from the sea. However, we discarded the regional influence on OCS  
508 transport because the urban sampling locations were surrounded by buildings. Instead, we  
509 assume that local winds have a higher weight on OCS transport, and we were not able to  
510 measure any significant local winds.

500

601 a) Sagrada Familia





611 **Fig. 6.** OCS enhancement ( $\Delta$  OCS) in ppt and calculated as measured OCS minus background  
 612 OCS (484 ppt for May and 407 ppt for October) for each campaign at the two urban parks as  
 613 follows: a) Sagrada Familia and b) Poblenou. The black arrow shows the wind direction and  
 614 speed measured on site, and the absence of an arrow indicates that there was no wind  
 615 blowing at the moment of measurement. A small map embedded in the lower right-hand  
 616 corner of each panel shows the residence time on a logarithmic scale of the air masses arriving  
 617 at the sampling site and determined with the FLEXPART model.

619 During the October campaign, there were no more mobility restrictions, and vehicle use was  
 620 back to business as usual. OCS concentrations were higher than background values in both  
 621 urban areas, as shown in the lower panels of Fig. 6. In the Sagrada Familia, the downwind  
 622 location at 7:00 UTC had a record-high  $\Delta$ OCS of +150 ppt, which was most likely capturing a  
 623 local source of OCS since the close-by target and upwind sites registered + 7 and -7 ppt,  
 624 respectively. The FLEXPART model indicates an influence of air mass with long residence  
 625 coming from the city, which together with a low PBL (approximately 30 m) and the absence of  
 626 local winds suggests that this peak of OCS is due to a nearby source of emission that was not

619 present for the other two sampling sites. At 9:30 UTC, the air transport regime changes, and  
620 we observe a marine influence. The PBL development increases to 1085 m, and we also  
621 observe an increase in local winds (Fig. 6). Even in the midst of this increased air mixture and  
622 neutral OCS transport,  $\Delta$ OCS increases up to 57 ppt, which points to local OCS sources in this  
623 urban area.

624 The other urban site, Poble Nou, did not exhibit such clear behavior of local OCS sources  
625 during October.  $\Delta$ OCS were -17, -16 and +25 ppt at 7:00 UTC and 0, -16 and +70 ppt at 9:30  
626 UTC for upwind, target, and downwind locations, respectively. The air masses were predicted  
627 to be influenced by regional sources, as FLEXPART suggests low residential periods in the urban  
628 area. There was moderate vertical air mixing (PBLH from 200 m at 7:00 UTC to 500 m at 9:30  
629 UTC) and weak atmospheric stability (Table 1).

630 **Agricultural:** The Gavà and El Prat sampling sites are located in the Llobregat River basin,  
631 which is mostly dedicated to peri-urban agriculture. Of the 5,500 ha of urban agricultural land  
632 at the AMB, over 2,800 ha are in this basin, as shown in Fig. 1. The main agricultural products  
633 grown in this area are horticultural crops (such as lettuce, tomatoes, peppers, and artichokes),  
634 herbaceous crops, fruits, and some cereals (such as barley and alfalfa), and many short-cycle  
635 crops that are interannually rotated and well irrigated. Only the upwind site of Gavà is on the  
636 coast alongside the built infrastructure and urban forest and outside an agricultural field (see  
637 supporting information Appendix S2 for pictures). The El Prat airport is nearby and between 3  
638 and 5 km east to El Prat and Gavà, respectively. Gavà values were a clear example of how the  
639 wind component affected OCS mixing ratios since it is surrounded by the sea (south),  
640 agricultural and natural land (west to north) and is influenced by the port and the airport to  
641 the east.

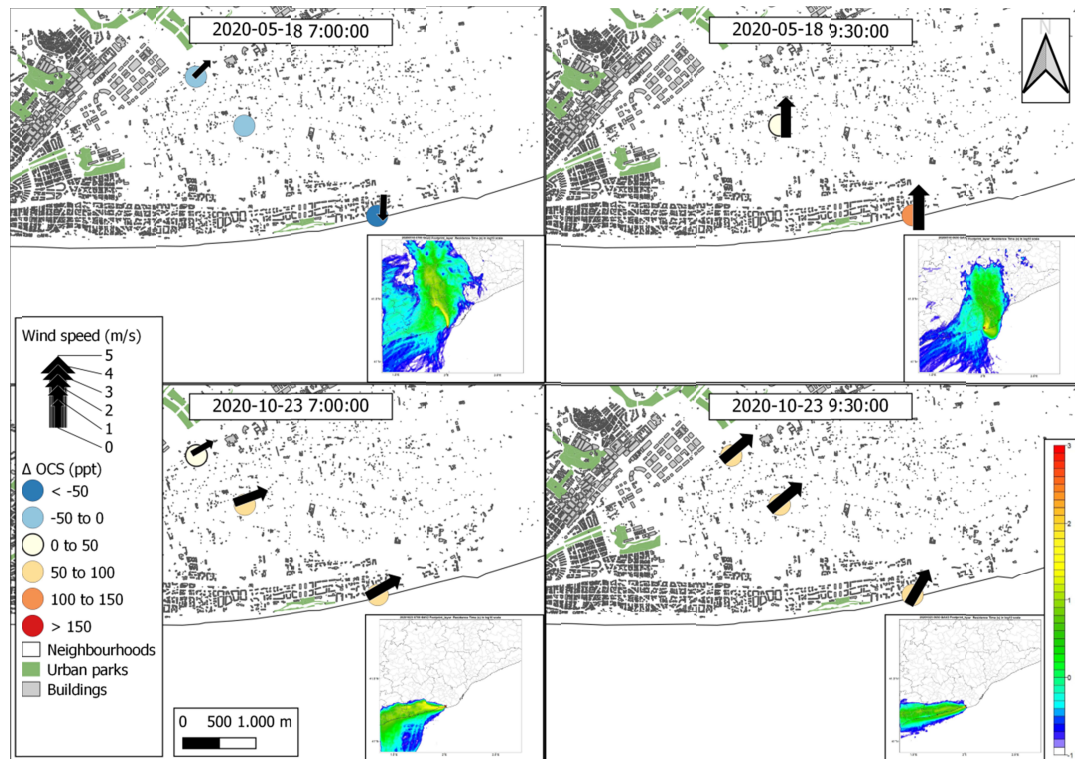
642 Fig. 7a shows low OCS concentrations well below the background values with  $\Delta$ OCS of -67, -  
643 +52, and -32 at 7:00 UTC in May during full photosynthetic activity of grown herbaceous fields,

644 which indicates the drawdown of OCS by vegetation. The wind measured on site was mostly  
645 from the north, especially for the downwind site, as confirmed with the FLEXPART trajectory,  
646 which predicts a high residential time for air masses coming from the north where the  
647 agricultural fields are located. This indicates that the OCS drawdown might not be entirely a  
648 local effect of agriculture but could also be due to a more regional effect of COS taken up by  
649 soil and vegetation during the night all over Catalonia and then advected by the land breeze  
650 over the AMB. However, by 9:30 UTC, OCS concentrations increased (up to an  $\Delta$ OCS of +116  
651 for the downwind site) when air masses were coming from the urban and port areas and  
652 despite PBLH development, which reached 1380 m that morning. During the October  
653 campaign, southwesterly winds predominated both at 7:00 and 9:30 UTC, which brought in air  
654 masses from the port and Gavà urban area with high industrial activity resulting in  $\Delta$ OCS  
655 between +82 and +40 ppt at 7:00 UTC. At 9:30 UTC,  $\Delta$ OCS values decreased slightly and had  
656 less variability ranging from +49 to +55 ppt, and this indicated a more homogenous air mixture  
657 due to a more developed PBL, which increased from 21-84 to 380-519 m for that location.  
658 During October, air transport had much more influence on the OCS budget than the  
659 agricultural land use as it did during the May campaign when the fields were in full  
660 photosynthetic activity.

661 The opposite behavior was observed at the El Prat agricultural site, where a deep PBLH (1200  
662 m) and regional air mass influence occurred in May, while a more stable situation and lower  
663 PBLH (691 m) dominated in October. In general, the values were similar to the background OCS  
664 for May with  $\Delta$ OCS values of +25, +37, and +22 ppt at 7:00 UTC and even higher enhancements  
665 at 9:30 (+17, +44 and +173 ppt, Fig. 7b). FLEXPART back trajectories in May showed air masses  
666 coming from the east with longer residential times located in the sea but still received  
667 influence from the airport and the port of Barcelona. During the October campaign, El Prat had  
668 higher OCS enhancements at both sampling times ( $\Delta$ OCS of +70, +33 and +80 ppt for 7:00 UTC;  
669 +7, +122 and +77 ppt for 9:30 UTC), which, given the low PBLH, suggests a local OCS source.

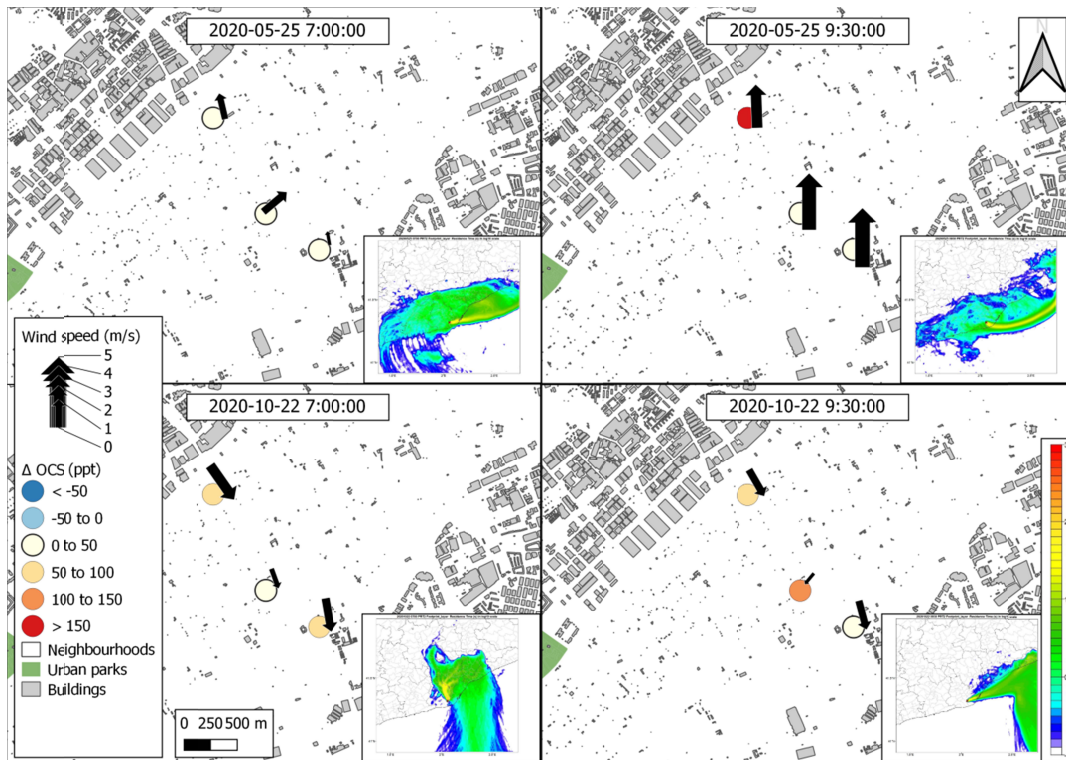
675 The FLEXPART showed that air masses came from the east indicating marine influence and/or  
676 from the port of Barcelona, where activities, such as air navigation and maritime traffic, had  
677 recovered 100% after the lockdown. The lower OCS concentrations in May compared to  
678 October highlight the significant sink of agriculture during the growing season as was seen for  
679 the Gavà location.

676 A) Gavà



677

678 B) El Prat



679

686 **Fig. 7.** OCS enhancement ( $\Delta$  OCS) in ppt calculated as the measure of OCS minus background  
 687 OCS (484 ppt for May and 407 ppt for October) for each campaign at the two urban parks as  
 688 follows: a) Gavà and b) El Prat. The black arrow shows the wind direction and speed measured  
 689 on site, and the absence of an arrow indicates that there was no wind blowing at the moment  
 690 of measurement. A small map embedded in the lower right-hand corner of each panel shows  
 691 the residence time on a logarithmic scale of the air masses arriving at the sampling site as  
 692 determined with the FLEXPART model.

#### 687 4.2. Considerations for OCS studies in urban ecosystems

693 Anthropogenic emissions are the primary source of OCS on a planetary scale, followed by  
 694 oceanic flux (Remaud et al., 2023), they are significant at the local and urban scales. In our  
 695 study, the peaks of OCS concentrations were mostly due to air masses coming from the port or  
 696 the city, as was the case for Montjuic in October or Gavà during the May campaign, and  
 697 reached values of 665 ppt for Montjuic and 600 ppt for Gavà (up to  $\Delta$ OCS of +258 and +193  
 698 ppt, respectively).

696 There are various potential sources of OCS in urban areas, such as the erosion of automobile  
 697 tires against asphalt, vehicle exhaust fumes, natural gas combustion and industrial processes  
 698 including oil refineries and aluminum production (Yan et al., 2019). In fact, in their inventory,

696 Yan et al. quantified the total emissions in 2015 for China alone as 174 Gg S yr<sup>-1</sup> with the  
697 highest contributions coming from industrial OCS emission processes (120 Gg S yr<sup>-1</sup>). In that  
698 same study, the total vehicle exhaust was responsible for 3 Gg S yr<sup>-1</sup>, which is approximately  
699 half of the yearly global estimate of 6 Gg S yr<sup>-1</sup> given by Lee and Brimblecombe (2016). The  
700 latter study also indicated that the heavy fuel oil used in ships is a significant source of the OCS  
701 budget and produces 30 Gg S yr<sup>-1</sup>. The AMB qualifies for all these potential sources and it has a  
702 heavily transited marine port that also has a combined cycle gas turbine power plant that runs  
703 on natural gas as well as an intense use of private vehicles within the city.

704 Additionally, a broad variety of sulfides are produced by wastewater where volatile organic  
705 compounds (VOC) such as MeSH, DMS, CS<sub>2</sub>, DMDS, DMTS and OCS are generated in anoxic  
706 environments of sewers (Lee and Brimblecombe, 2016), and it has been noted that the  
707 microbial activity in these anoxic sediments is closely linked to the production of OCS (Kitz et  
708 al., 2019). Sulfide emissions from urban wastewater networks are frequently detected due to  
709 their bad odor as is the case for Barcelona (Eijo-Río et al., 2015) and Thessaloniki (Besis et al.,  
710 2021). In our study, the sampling sites of Sagrada Familia in October ( $\Delta$ OCS of +150 ppt) and  
711 Poble Nou ( $\Delta$ OCS of +50 ppt) concur with locations of a combined sewer system previously  
712 reported to have high peaks of H<sub>2</sub>S, which indicated a potential OCS source from wastewater.  
713 Unfortunately, constraining this signal from other potential urban sources was out of the  
714 scope of this study.

715 In terms of vegetated land uses, we found one case of a significant OCS drawdown in  
716 agricultural sites during the growing season of May. In addition to photosynthetic uptake  
717 (Campbell et al., 2017, 2008; Montzka et al., 2007), waterlogged soils have been reported to  
718 act as sinks of OCS when planted with crops (Yi et al., 2008). The agricultural fields of the  
719 Llobregat basin are mostly irrigated by inundation, which could further intensify the OCS  
720 uptake and explain the OCS drawdown at 7:00 UTC when photosynthetic activity was high. We

721 also found values indicating uptake during the growing season in Collserola Forest, which is in  
722 agreement with other studies evaluating forest OCS uptake (Belviso et al., 2016; Campbell et  
723 al., 2017, 2008).

724 Finally, determining the influence of land use on the overall urban OCS budget requires a  
725 reliable background measurement. In general, background levels for OCS are associated with  
726 air masses coming from the sea because the stability provided by oceans results in constant  
727 OCS concentrations, at least at a seasonal scale (Montzka et al., 2007), as was the case for San  
728 Francisco (Villalba et al., 2021). However, this is not applicable for the AMB because the  
729 convection regime is quite peculiar. The AMB has a unique land–sea air mass exchange in  
730 which sea breezes under specific conditions do not bring new air masses but rather recycle air  
731 masses that originated over the urban area, however, a deeper research should be done in this  
732 regard, since marine contribution cannot be neglected. This type of process has been observed  
733 by Jaén et al. (2021), who described how ozone plumes stay over the shore due to advective  
734 processes during heat episodes such as heatwaves. The thermal component of convective  
735 processes creating episodes of air recirculation on the Spanish eastern coast has also been  
736 documented by Millán et al. (2000), where they outline how the sea breeze can favor the  
737 formation of layers of stratified air reservoirs in heights where compounds accumulate that  
738 can later return to the land. This particular sea breeze circulation constricts local ventilation  
739 and exacerbates the accumulation of anthropogenic gases emitted in the AMB.

740

## 741 **5. Conclusions**

742 We performed two measurement campaigns of OCS mixing ratios in the Metropolitan Area of  
743 Barcelona (AMB) to explore to what extent different urban land uses can have an impact on  
744 the OCS mixing ratios measured on flask samples regarding a particular urban climate,  
745 geography, and topography of AMB. Air samples were taken at locations representing four

746 different land uses as follows: urban parks, forests, agricultural fields and impervious urban  
747 landscapes.

748 Based on the interflask comparison described in 2.3, we determined that the OCS  
749 measurement uncertainty can be as high as +53 ppt, which reflects that near-surface  
750 measurements in urban heterogeneous environments result in higher uncertainties than in  
751 homogenous rural environments. We also compared average OCS concentrations  $\pm\sigma$  with  
752 values observed from ICOS- LSCE in Gif-sur-Yvette (GIF), which were taken at the same moment  
753 as our campaign (Fig. S3). We observed how mean OCS concentrations and  $\sigma$  in the AMB were  
754 systematically higher than in GIF, which suggests that anthropogenic emissions could affect  
755 the increase in uncertainty.

756 The ability to capture a photosynthetic signal appears weak in vegetated areas within the city,  
757 such as parks, and is relegated to forests and peri-urban agricultural areas. Urban parks  
758 showed values significantly higher than the established background value, both in May (i.e., up  
759 to +144 ppt) and in October (i.e., up to +150 ppt), which shows the influence of anthropogenic  
760 sources, possibly from the port and the city center, which masks the possibility of capturing  
761 the signal from the vegetation. The urban forest suggested OCS uptake values up to -33 ppt,  
762 which indicates a significant photosynthesis sink in denser vegetation masses even within city  
763 limits.

764 The urban area showed a variety of signals from almost neutral to above the background  
765 value, which suggests nearby emission sources. In our case, we found the explanation of some  
766 process values that may be aligned with urban traffic but above all with the industrial activity  
767 of the port and airport (for example, high OCS values in Montjuic when the wind came directly  
768 from the port). We can also think of other biogenic processes that produce OCS processes  
769 linked to human activity on urban land such as the waste system. These processes should be  
770 studied in more detail in future works. We have not been able to capture an effect of urban

771 vegetation on OCS uptake; instead, the peri-urban area of agriculture and forests may have  
772 more important roles in the OCS dynamics in cities.

773 Last, agricultural areas showed a clear drawdown during the growing season for the location of  
774 Gavà, where we were able to discard regional influences and intense air mixing. OCS  
775 enhancements in October reflect the loss of photosynthetic uptake and the return to business  
776 as usual traffic and nearby airport and port activities.

777 Overall, the variability of OCS in the urban ecosystem was higher than we expected. The  
778 URBAG campaigns of OCS measurements showed evidence that the use of OCS as a trace gas  
779 to determine the contribution of the urban biosphere to the CO<sub>2</sub> budget is a complicated task  
780 and that the vegetation signal is difficult to detect because local anthropogenic activities have  
781 a significant influence. The urban ecosystem is complex in terms of land uptake, marine  
782 emissions, and anthropogenic emissions from the city port, and strongly impacts the spatial-  
783 temporal distribution of OCS in the AMB and impedes a clear constraint of the biosphere  
784 signal.

#### 785 **Acknowledgments**

786 This work has been made possible thanks to the financial support of the European Research  
787 Council (ERC) Consolidator project: Integrated System Analysis of Urban Vegetation and  
788 Agriculture (818002-URBAG), the Spanish Ministry of Science, Innovation and Universities,  
789 through the “Maria de Maeztu” programme for Units of Excellence (CEX2019-000940-M), and  
790 the funding and recognition awarded to the research group Sostenipra (2021 SGR 00734) by  
791 the Department of Research and Universities of the Generalitat de Catalunya. This work also  
792 has been granted by the Spanish Ministry of Science and Innovation MCIN  
793 AEI/10.13039/501100011033 under contract PID2020-113614RB-C21, by the Spanish  
794 government under grant PRE2018-085425 and by the Catalan government under contract  
795 2021 SGR 00574.

796 **Open Research Section**

797 The data acquired during the URBAG measurement campaigns used for the analysis of land  
798 influence in this study are available at ZENODO via <https://doi.org/10.5281/zenodo.8072833>  
799 with Creative Commons Attribution 4.0 International license.

800 **References:**

- 801 Badia, A., Langemeyer, J., Codina, X., Gilabert, J., Guilera, N., Vidal, V., Segura, R., Vives, M.,  
802 Villalba, G., 2021. A take-home message from COVID-19 on urban air pollution reduction  
803 through mobility limitations and teleworking. *npj Urban Sustain.* 1.  
804 <https://doi.org/10.1038/s42949-021-00037-7>
- 805 Belviso, S., Abadie, C., Montagne, D., Hadjar, D., Tropée, D., Vialettes, L., Kazan, V., Delmotte,  
806 M., Maignan, F., Remaud, M., Ramonet, M., Lopez, M., Yver-Kwok, C., Ciais, P., 2022.  
807 Carbonyl sulfide (COS) emissions in two agroecosystems in central France. *PLoS One* 17,  
808 1–15. <https://doi.org/10.1371/journal.pone.0278584>
- 809 Belviso, S., Pison, I., Petit, J.E., Berchet, A., Remaud, M., Simon, L., Ramonet, M., Delmotte, M.,  
810 Kazan, V., Yver-Kwok, C., Lopez, M., 2023. The Z-2018 emissions inventory of COS in  
811 Europe: A semiquantitative multi-data-streams evaluation. *Atmos. Environ.* 300, 119689.  
812 <https://doi.org/10.1016/j.atmosenv.2023.119689>
- 813 Belviso, S., Reiter, I.M., Loubet, B., Gros, V., Lathière, J., Montagne, D., Delmotte, M., Ramonet,  
814 M., Kalogridis, C., Lebegue, B., Bonnaire, N., Kazan, V., Gauquelin, T., Fernandez, C.,  
815 Genty, B., 2016. A top-down approach of surface carbonyl sulfide exchange by a  
816 Mediterranean oak forest ecosystem in southern France. *Atmos. Chem. Phys.* 16, 14909–  
817 14923. <https://doi.org/10.5194/acp-16-14909-2016>
- 818 Besis, A., Georgiadou, E., Samara, C., 2021. Odor-active volatile organic compounds along the

819            seafront of Thessaloniki, Greece. Implications for sources of nuisance odor. *Sci. Total*  
820            *Environ.* 799, 149388. <https://doi.org/10.1016/j.scitotenv.2021.149388>

821 Brioude, J., Arnold, D., Stohl, A., Cassiani, M., Morton, D., Seibert, P., Angevine, W., Evan, S.,  
822            Dingwell, A., Fast, J.D., Easter, R.C., Pisso, I., Burkhardt, J., Wotawa, G., 2013. The  
823            Lagrangian particle dispersion model FLEXPART-WRF version 3.1. *Geosci. Model Dev.* 6.  
824            <https://doi.org/10.5194/gmd-6-1889-2013>

825 Campbell, J.E., Carmichael, G.R., Chai, T., Mena-Carrasco, M., Tang, Y., Blake, D.R., Blake, N.J.,  
826            Vay, S.A., Collatz, G.J., Baker, I., Berry, J.A., Montzka, S.A., Sweeney, C., Schnoor, J.L.,  
827            Stanier, C.O., T. Chai, M., Mena-Carrasco, Y., Tang, D.R., Blake, N.J., Blake, S.A., Vay, G.J.,  
828            Collatz, I., Baker, J.A., Berry, S.A., Montzka, C., Sweeney, J.L., And, S., Stanier, C.O., 2008.  
829            Photosynthetic Control of Atmospheric Carbonyl Sulfide During the Growing Season.  
830            *Science* (80-. ). 1085–1088. <https://doi.org/10.1126/science.1164015>

831 Campbell, J.E., Whelan, M.E., Berry, J.A., Hilton, T.W., Zumkehr, A., Stinecipher, J., Lu, Y.,  
832            Kornfeld, A., Seibt, U., Dawson, T.E., Montzka, S.A., Baker, I.T., Kulkarni, S., Wang, Y.,  
833            Herndon, S.C., Zahniser, M.S., Commane, R., Loik, M.E., 2017. Plant Uptake of  
834            Atmospheric Carbonyl Sulfide in Coast Redwood Forests. *J. Geophys. Res. Biogeosciences*  
835            122, 3391–3404. <https://doi.org/10.1002/2016JG003703>

836 Commane, R., Herndon, S.C., Zahniser, M.S., Lerner, B.M., McManus, J.B., Munger, J.W.,  
837            Nelson, D.D., Wofsy, S.C., 2013. Carbonyl sulfide in the planetary boundary layer: Coastal  
838            and continental influences. *J. Geophys. Res. Atmos.* 118.  
839            <https://doi.org/10.1002/jgrd.50581>

840 Copernicus, 2023. ERA5 hourly data on single levels from 1940 to present [WWW Document].  
841            URL [https://cds.climate.copernicus.eu/cdsapp#!/dataset/reanalysis-era5-single-](https://cds.climate.copernicus.eu/cdsapp#!/dataset/reanalysis-era5-single-levels?tab=overview)  
842            [levels?tab=overview](https://cds.climate.copernicus.eu/cdsapp#!/dataset/reanalysis-era5-single-levels?tab=overview) (accessed 5.21.23).

843 Eijo-Río, E., Petit-Boix, A., Villalba, G., Suárez-Ojeda, M.E., Marin, D., Amores, M.J., Aldea, X.,  
844 Rieradevall, J., Gabarrell, X., 2015. Municipal sewer networks as sources of nitrous oxide,  
845 methane and hydrogen sulphide emissions: A review and case studies. *J. Environ. Chem.*  
846 *Eng.* <https://doi.org/10.1016/j.jece.2015.07.006>

847 Garcia-Dalmau, M., Udina, M., Bech, J., Sola, Y., Montolio, J., Jaén, C., 2021. Pollutant  
848 Concentration Changes During COVID-19 Lockdown in Barcelona and Surrounding Region:  
849 Modification of Diurnal Cycles and Limited Role of Meteorological Conditions In press.

850 GCOS, 2016. The Global Observing System For Climate Implementation Needs. *World*  
851 *Meteorol. Organ.* 200.

852 Gilabert, J., Ventura, S., Segura, R., Martilli, A., Badia, A., Llasat, C., Corbera, J., Villalba, G.,  
853 2021. Abating heat waves in a coastal Mediterranean city: What can cool roofs and  
854 vegetation contribute? *Urban Clim.* 37, 100863.  
855 <https://doi.org/10.1016/J.UCLIM.2021.100863>

856 Griffiths, A.D., Parkes, S.D., Chambers, S.D., McCabe, M.F., Williams, A.G., 2013. Improved  
857 mixing height monitoring through a combination of lidar and radon measurements.  
858 *Atmos. Meas. Tech.* 6. <https://doi.org/10.5194/amt-6-207-2013>

859 Grossi, C., Arnold, D., Adame, J.A., López-Coto, I., Bolívar, J.P., De La Morena, B.A., Vargas, A.,  
860 2012. Atmospheric <sup>222</sup>Rn concentration and source term at El Arenosillo 100 m  
861 meteorological tower in southwest Spain. *Radiat. Meas.* 47.  
862 <https://doi.org/10.1016/j.radmeas.2011.11.006>

863 Guevara, M., Jorba, O., Soret, A., Petetin, H., Bowdalo, D., Serradell, K., Tena, C., Van Der Gon,  
864 H.D., Kuenen, J., Peuch, V.H., Pérez Garcíá-Pando, C., 2021. Time-resolved emission  
865 reductions for atmospheric chemistry modelling in Europe during the COVID-19  
866 lockdowns. *Atmos. Chem. Phys.* 21. <https://doi.org/10.5194/acp-21-773-2021>

867 Holzworth, G.C., 1964. Estimates of mean maximum mixing depths in the contiguous united  
868 states. *Mon. Weather Rev.* 92. [https://doi.org/10.1175/1520-](https://doi.org/10.1175/1520-0493(1964)092<0235:eommmmd>2.3.co;2)  
869 [0493\(1964\)092<0235:eommmmd>2.3.co;2](https://doi.org/10.1175/1520-0493(1964)092<0235:eommmmd>2.3.co;2)

870 Institut d'Estadística de Catalunya, 2023. Idescat [WWW Document]. URL  
871 <https://www.idescat.cat/> (accessed 5.21.23).

872 Jaén, C., Udina, M., Bech, J., 2021. Analysis of two heat wave driven ozone episodes in  
873 Barcelona and surrounding region: Meteorological and photochemical modeling. *Atmos.*  
874 *Environ.* 246. <https://doi.org/10.1016/j.atmosenv.2020.118037>

875 Kitz, F., Gómez-Brandón, M., Eder, B., Etemadi, M., Spielmann, F.M., Hammerle, A., Insam, H.,  
876 Wohlfahrt, G., 2019. Soil carbonyl sulfide exchange in relation to microbial community  
877 composition: Insights from a managed grassland soil amendment experiment. *Soil Biol.*  
878 *Biochem.* 135, 28–37. <https://doi.org/10.1016/j.soilbio.2019.04.005>

879 Lee, C.L., Brimblecombe, P., 2016. Anthropogenic contributions to global carbonyl sulfide,  
880 carbon disulfide and organosulfides fluxes. *Earth-Science Rev.* 160, 1–18.  
881 <https://doi.org/10.1016/J.EARSCIREV.2016.06.005>

882 Leelőssy, Á., Mona, T., Mészáros, R., Lagzi, I., Havasi, Á., 2016. Eulerian and Lagrangian  
883 Approaches for Modelling of Air Quality. [https://doi.org/10.1007/978-3-319-40157-7\\_5](https://doi.org/10.1007/978-3-319-40157-7_5)

884 Liu, S., Liang, X.-Z., 2010. Observed Diurnal Cycle Climatology of Planetary Boundary Layer  
885 Height. *J. Clim.* 23, 5790–5809. <https://doi.org/10.1175/2010JCLI3552.1>

886 Lotteraner, C., Piringer, M., 2016. Mixing-Height Time Series from Operational Ceilometer  
887 Aerosol-Layer Heights. *Boundary-Layer Meteorol.* 161. [https://doi.org/10.1007/s10546-](https://doi.org/10.1007/s10546-016-0169-2)  
888 [016-0169-2](https://doi.org/10.1007/s10546-016-0169-2)

889 Mallik, C., Chandra, N., Venkataramani, S., Lal, S., 2016. Variability of atmospheric carbonyl

890 sulfide at a semi-arid urban site in western India. *Sci. Total Environ.* 551–552.  
891 <https://doi.org/10.1016/j.scitotenv.2016.02.014>

892 Millán, M.M., Mantilla, E., Salvador, R., Carratalá, A., Sanz, M.J., Alonso, L., Gangoiti, G.,  
893 Navazo, M., 2000. Ozone cycles in the western Mediterranean basin: Interpretation of  
894 monitoring data in complex coastal terrain. *J. Appl. Meteorol.* 39.  
895 [https://doi.org/10.1175/1520-0450\(2000\)039<0487:OCITWM>2.0.CO;2](https://doi.org/10.1175/1520-0450(2000)039<0487:OCITWM>2.0.CO;2)

896 Montzka, S.A., Calvert, P., Hall, B.D., Elkins, J.W., Conway, T.J., Tans, P.P., Sweeney, C.S., 2007.  
897 On the global distribution, seasonality, and budget of atmospheric carbonyl sulfide (COS)  
898 and some similarities to CO<sub>2</sub>. *J. Geophys. Res. Atmos.* 112, 1–15.  
899 <https://doi.org/10.1029/2006JD007665>

900 Protoschill-Krebs, G., Kesselmeier, J., 1992. Enzymatic Pathways for the Consumption of  
901 Carbonyl Sulphide (COS) by Higher Plants. *Bot. Acta* 105, 206–212.  
902 <https://doi.org/10.1111/j.1438-8677.1992.tb00288.x>

903 Querol, X., Alastuey, A., Ruiz, C.R., Artiñano, B., Hansson, H.C., Harrison, R.M., Buringh, E., Ten  
904 Brink, H.M., Lutz, M., Bruckmann, P., Straehl, P., Schneider, J., 2004. Speciation and origin  
905 of PM<sub>10</sub> and PM<sub>2.5</sub> in selected European cities. *Atmos. Environ.* 38, 6547–6555.  
906 <https://doi.org/10.1016/j.atmosenv.2004.08.037>

907 Remaud, M., Chevallier, F., Maignan, F., Belviso, S., Berchet, A., Parouffe, A., Abadie, C.,  
908 Bacour, C., Lennartz, S., Peylin, P., 2022. Plant gross primary production, plant respiration  
909 and carbonyl sulfide emissions over the globe inferred by atmospheric inverse modelling.  
910 *Atmos. Chem. Phys.* 22. <https://doi.org/10.5194/acp-22-2525-2022>

911 Remaud, M., Ma, J., Krol, M., Abadie, C., Cartwright, M.P., 2023. Intercomparison of  
912 Atmospheric Carbonyl Sulfide ( TransCom-COS ; Part One ): Evaluating the Impact of  
913 Transport and Emissions on Tropospheric Variability Using Ground-Based and Aircraft

914 Data Journal of Geophysical Research : Atmospheres 1–23.  
915 <https://doi.org/10.1029/2022JD037817>

916 Ribeiro, I., Martilli, A., Falls, M., Zonato, A., Villalba, G., 2021. Highly resolved WRF-BEP/BEM  
917 simulations over Barcelona urban area with LCZ. Atmos. Res. 248, 105220.  
918 <https://doi.org/10.1016/J.ATMOSRES.2020.105220>

919 Salamanca, F., Krpo, A., Martilli, A., Clappier, A., 2010. A new building energy model coupled  
920 with an urban canopy parameterization for urban climate simulations-part I. formulation,  
921 verification, and sensitivity analysis of the model. Theor. Appl. Climatol. 99.  
922 <https://doi.org/10.1007/s00704-009-0142-9>

923 Segura, R., Badia, A., Ventura, S., Gilabert, J., Martilli, A., Villalba, G., 2021. Sensitivity study of  
924 PBL schemes and soil initialization using the WRF-BEP-BEM model over a Mediterranean  
925 coastal city. Urban Clim. 39. <https://doi.org/10.1016/j.uclim.2021.100982>

926 Seibert, P., Beyrich, F., Gryning, S.E., Joffre, S., Rasmussen, A., Tercier, P., 2000. Review and  
927 intercomparison of operational methods for the determination of the mixing height.  
928 Atmos. Environ. [https://doi.org/10.1016/S1352-2310\(99\)00349-0](https://doi.org/10.1016/S1352-2310(99)00349-0)

929 Servei Meteorològic de Catalunya, 2023. El temps a Catalunya [WWW Document]. URL  
930 <https://www.meteo.cat/> (accessed 5.21.23).

931 Skamarock, W.C., Klemp, J.B., Dudhia, J., Gill, D.O., Liu, Z., Berner, J., Wang, W., Powers, J.G.,  
932 Duda, M.G., Barker, D., Huang, X., 2021. A Description of the Advanced Research WRF  
933 Model Version 4.3. <https://doi.org/10.5065/1dfh-6p97>

934 Stewart, I.D., Oke, T.R., 2012. Local climate zones for urban temperature studies. Bull. Am.  
935 Meteorol. Soc. 93. <https://doi.org/10.1175/BAMS-D-11-00019.1>

936 Stohl, A., Forster, C., Frank, A., Seibert, P., Wotawa, G., 2005. Technical note: The Lagrangian

937 particle dispersion model FLEXPART version 6.2. Atmos. Chem. Phys. 5.  
938 <https://doi.org/10.5194/acp-5-2461-2005>

939 Stull, R., 1988. An Introduction to Boundary Layer Meteorology. Kluwer Academic Publishers.

940 Sturm, P., Leuenberger, M., Sirignano, C., Neubert, R.E.M., Meijer, H.A.J., Langenfelds, R.,  
941 Brand, W.A., Tohjima, Y., 2004. Permeation of atmospheric gases through polymer O-  
942 rings used in flasks for air sampling. J. Geophys. Res. D Atmos. 109.

943 URBAG, 2023. Full dataset of carbonyl sulfide URBAG measurement campaign May and  
944 October 2020 [Data set]. Zenodo. <https://doi.org/10.5281/zenodo.8072833>

945 VAISALA, 2020. Investigation of Boundary Layer Structures with Ceilometer [WWW  
946 Document]. VAISALA. URL <https://www.vaisala.com/en/products/software/bl-view>

947 Villalba, G., Whelan, M., Montzka, S.A., Cameron-Smith, P.J., Fischer, M., Zumkehr, A., Hilton,  
948 T., Stinecpher, J., Baker, I., Bambha, R.P., Michelsen, H.A., LaFranchi, B.W., Estruch, C.,  
949 Campbell, E., 2021. Exploring the Potential of Using Carbonyl Sulfide to Track the Urban  
950 Biosphere Signal. J. Geophys. Res. Atmos. 126. <https://doi.org/10.1029/2020JD034106>

951 Whelan, M.E., Lennartz, S.T., Gimeno, T.E., Wehr, R., Wohlfahrt, G., Wang, Y., Kooijmans,  
952 L.M.J., Hilton, T.W., Belviso, S., Peylin, P., Commane, R., Sun, W., Chen, H., Kuai, L.,  
953 Mammarella, I., Maseyk, K., Berkelhammer, M., Li, K.F., Yakir, D., Zumkehr, A., Katayama,  
954 Y., Oge, J., Spielmann, F.M., Kitz, F., Rastogi, B., Kesselmeier, J., Marshall, J., Erkkila, K.M.,  
955 Wingate, L., Meredith, L.K., He, W., Bunk, R., Launois, T., Vesala, T., Schmidt, J.A., Fichot,  
956 C.G., Seibt, U., Saleska, S., Saltzman, E.S., Montzka, S.A., Berry, J.A., Elliott Campbell, J.,  
957 2018. Reviews and syntheses: Carbonyl sulfide as a multi-scale tracer for carbon and  
958 water cycles, Biogeosciences. <https://doi.org/10.5194/bg-15-3625-2018>

959 Yan, Y., Li, R., Peng, L., Yang, C., Liu, C., Cao, J., Yang, F., Li, Y., Wu, J., 2019. Emission inventory

960 of carbonyl sulfide (COS) from primary anthropogenic sources in China. *Environ. Pollut.*  
961 247, 745–751. <https://doi.org/10.1016/j.envpol.2019.01.096>

962 Yang, F., Qubaja, R., Tatarinov, F., Rotenberg, E., Yakir, D., 2018. Assessing canopy performance  
963 using carbonyl sulfide measurements. *Glob. Chang. Biol.* 24, 3486–3498.  
964 <https://doi.org/10.1111/gcb.14145>

965 Yi, Z., Wang, X., Sheng, G., Fu, J., 2008. Exchange of carbonyl sulfide (OCS) and dimethyl sulfide  
966 (DMS) between rice paddy fields and the atmosphere in subtropical China. *Agric. Ecosyst.*  
967 *Environ.* 123, 116–124. <https://doi.org/10.1016/j.agee.2007.05.011>

968 Yu, J., Steinberger, Y., 2011. Vertical Distribution of Microbial Community Functionality under  
969 the Canopies of *Zygophyllum dumosum* and *Hammada scoparia* in the Negev Desert,  
970 Israel. *Microb. Ecol.* 62, 218–227.

971 Zumkehr, A., Hilton, T.W., Whelan, M., Smith, S., Campbell, J.E., 2017. Gridded anthropogenic  
972 emissions inventory and atmospheric transport of carbonyl sulfide in the U.S. *J. Geophys.*  
973 *Res.* 122, 2169–2178. <https://doi.org/10.1002/2016JD025550>

974 Zumkehr, A., Hilton, T.W., Whelan, M., Smith, S., Kuai, L., Worden, J., Campbell, J.E., 2018.  
975 Global gridded anthropogenic emissions inventory of carbonyl sulfide. *Atmos. Environ.*  
976 183, 11–19. <https://doi.org/10.1016/j.atmosenv.2018.03.063>

977

Figure 1.

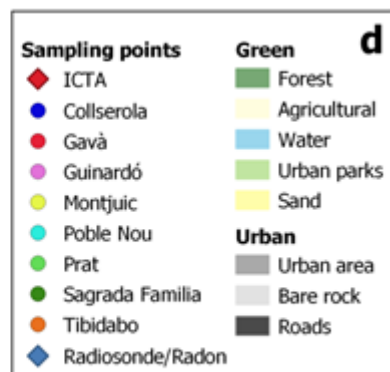
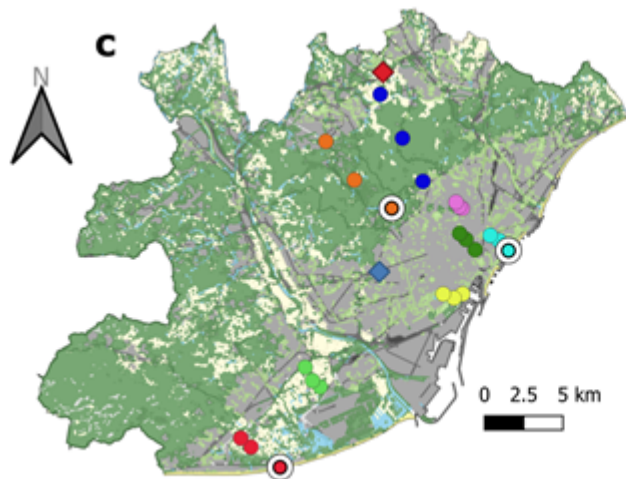
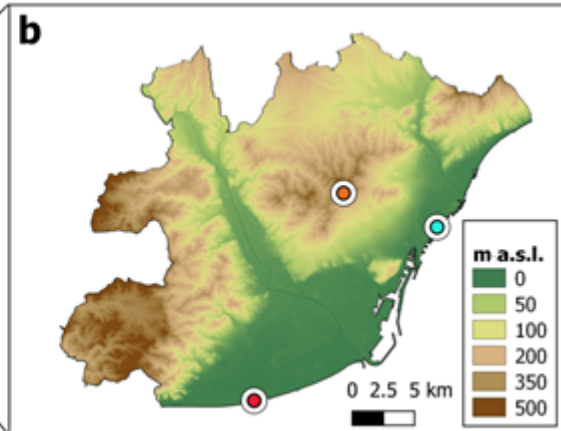


Figure 2.

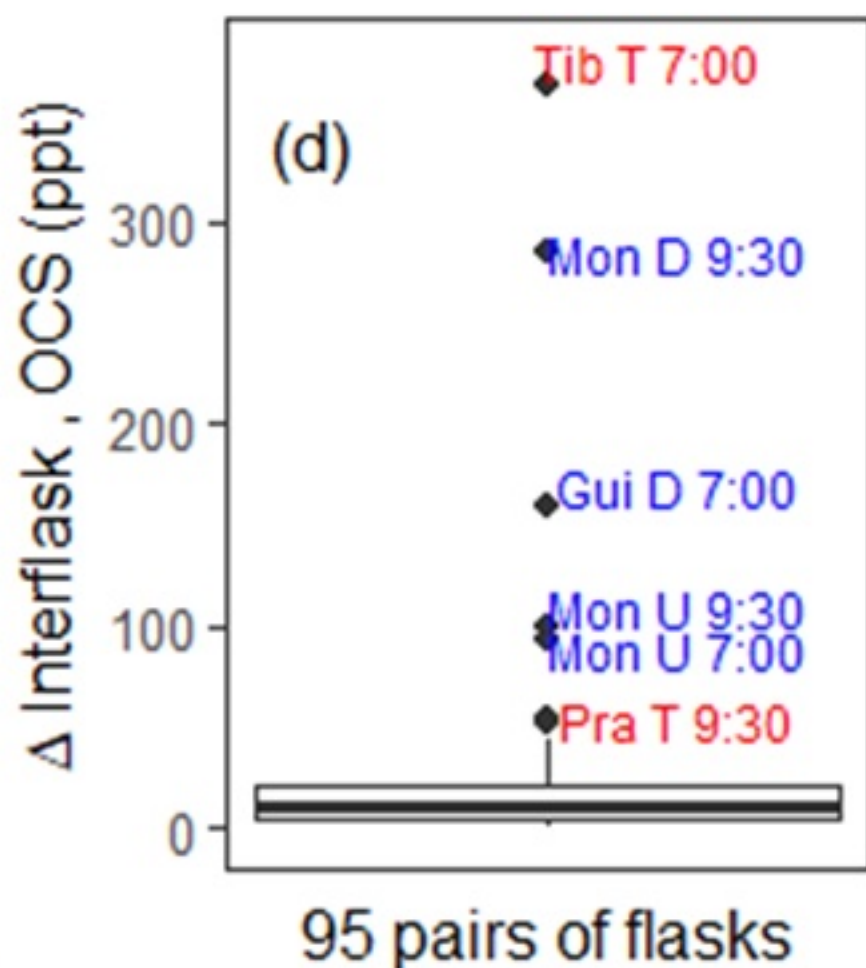
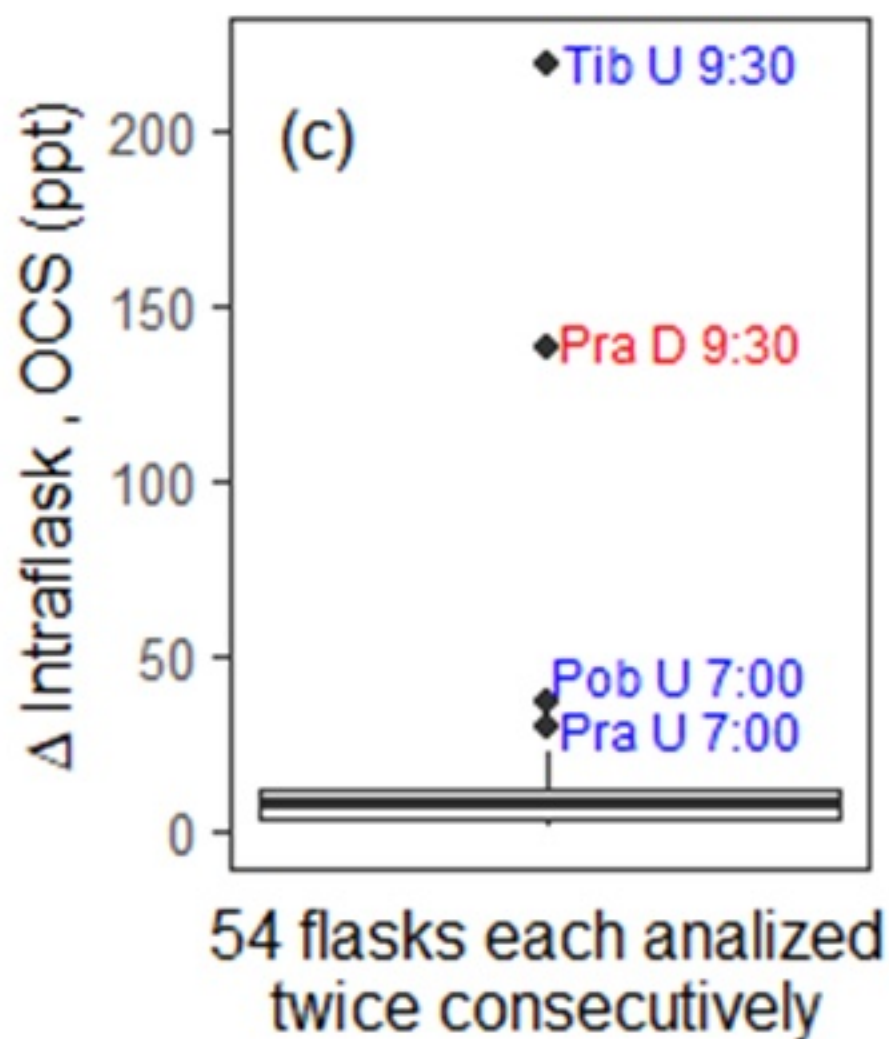
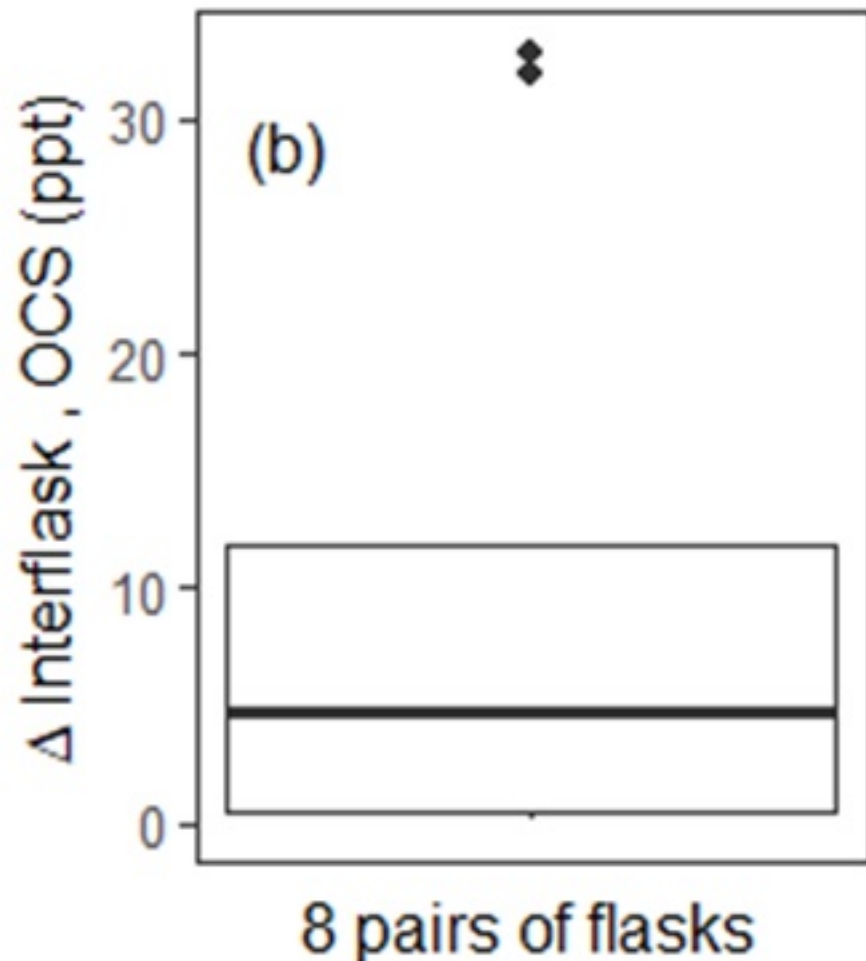
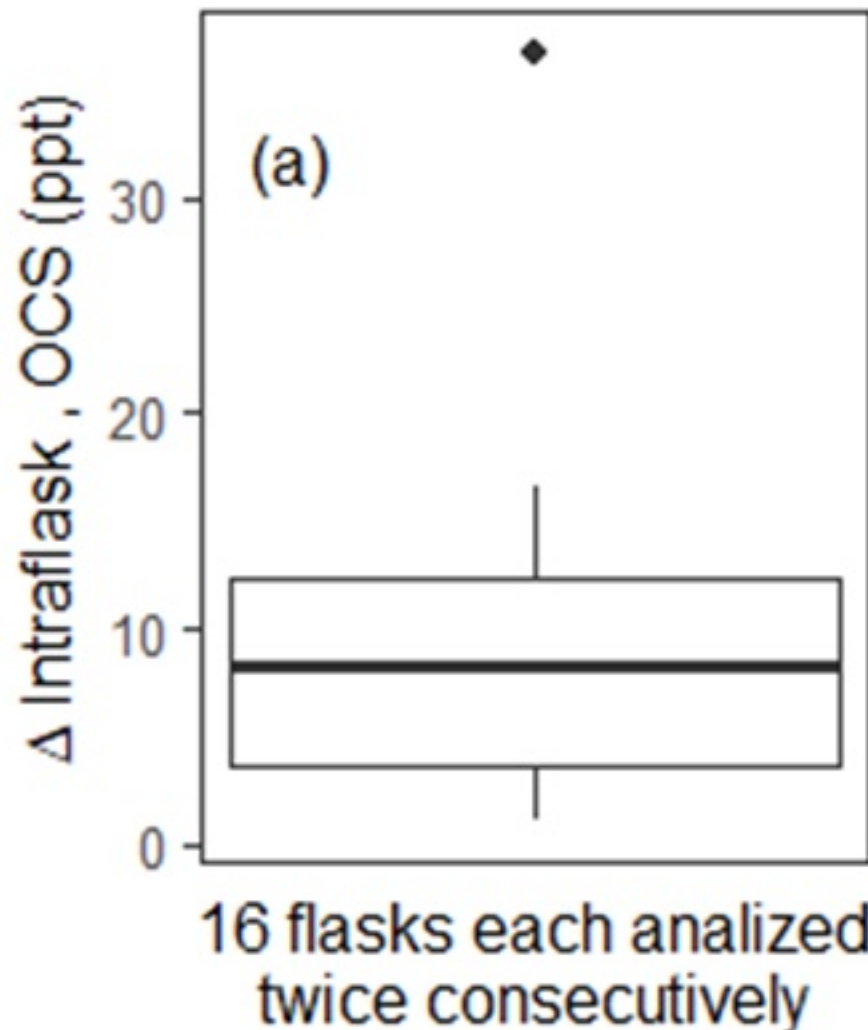


Figure 3.

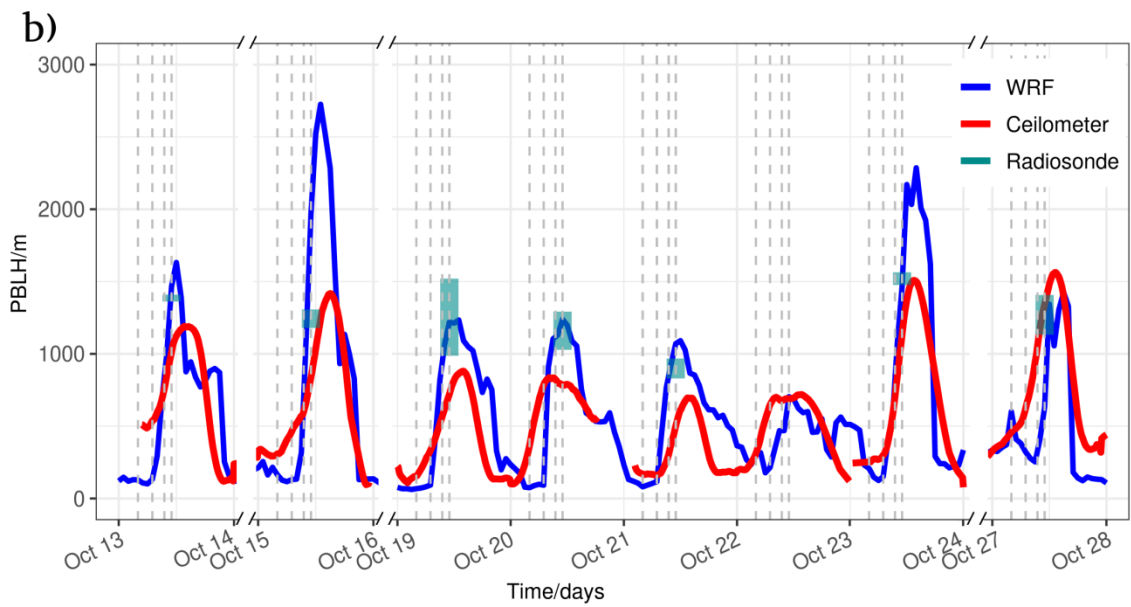
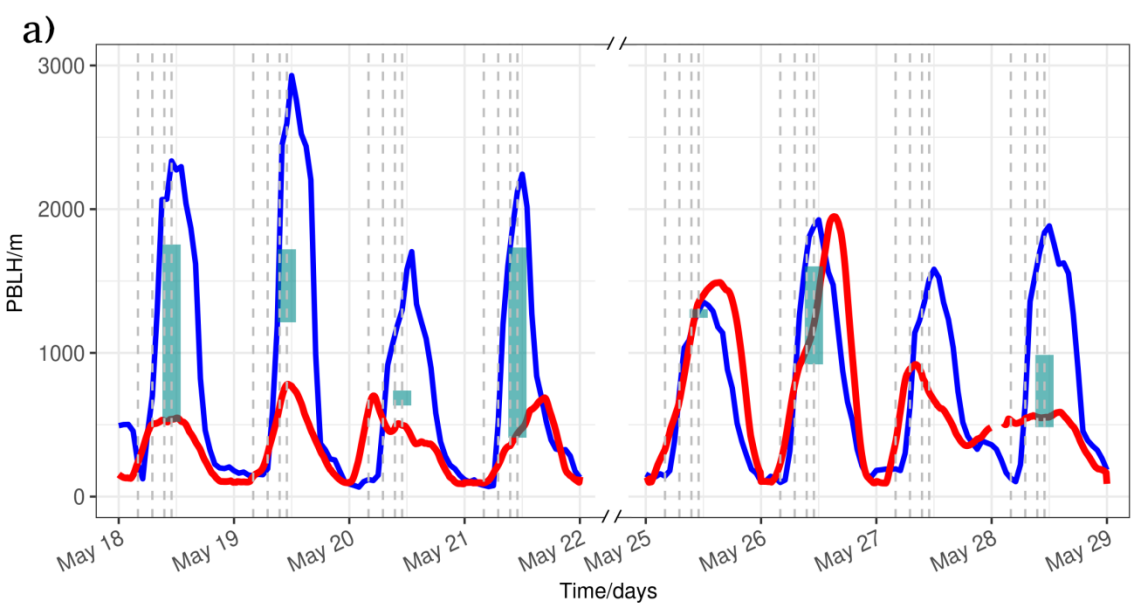


Figure 4.

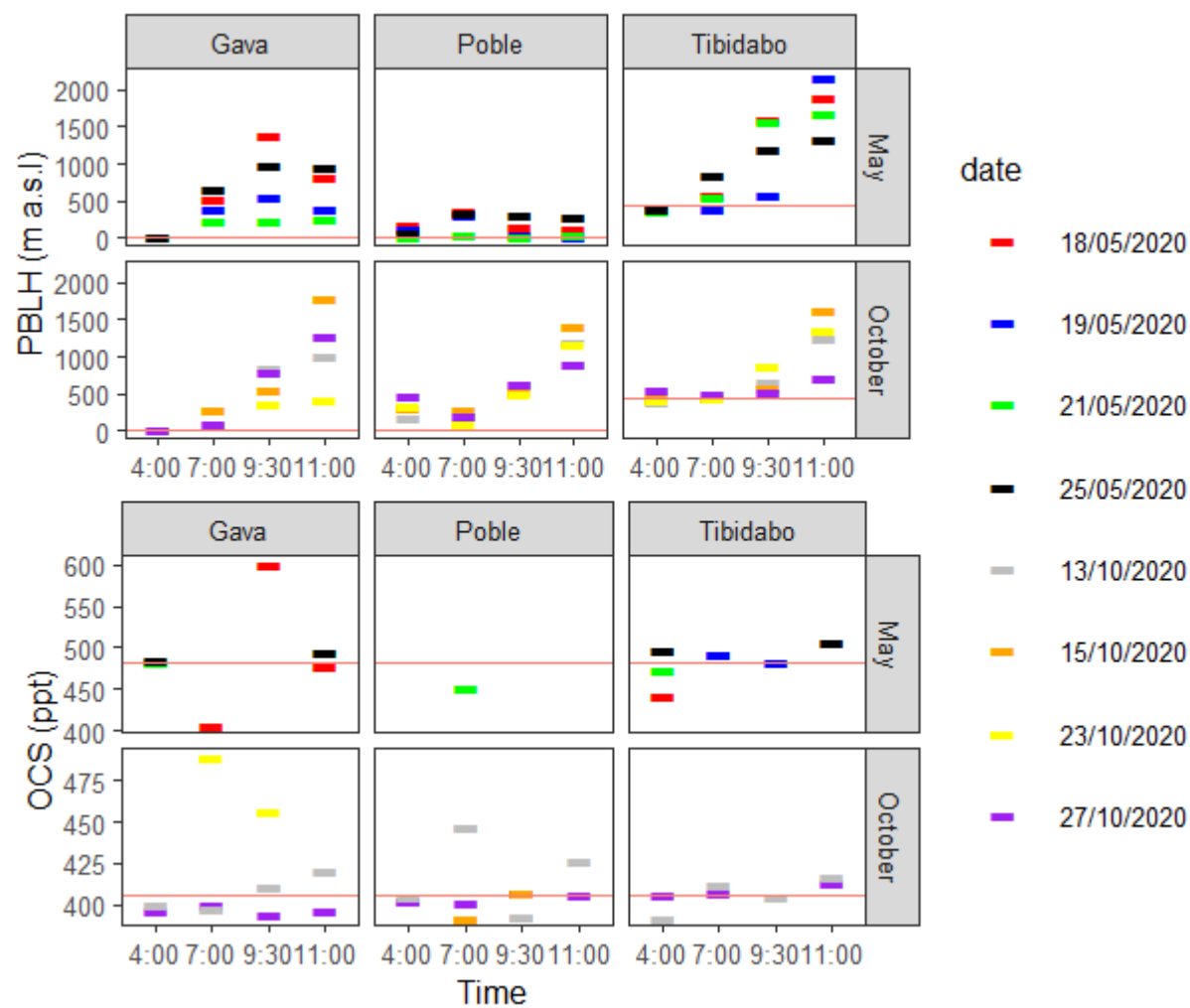


Figure 5a.

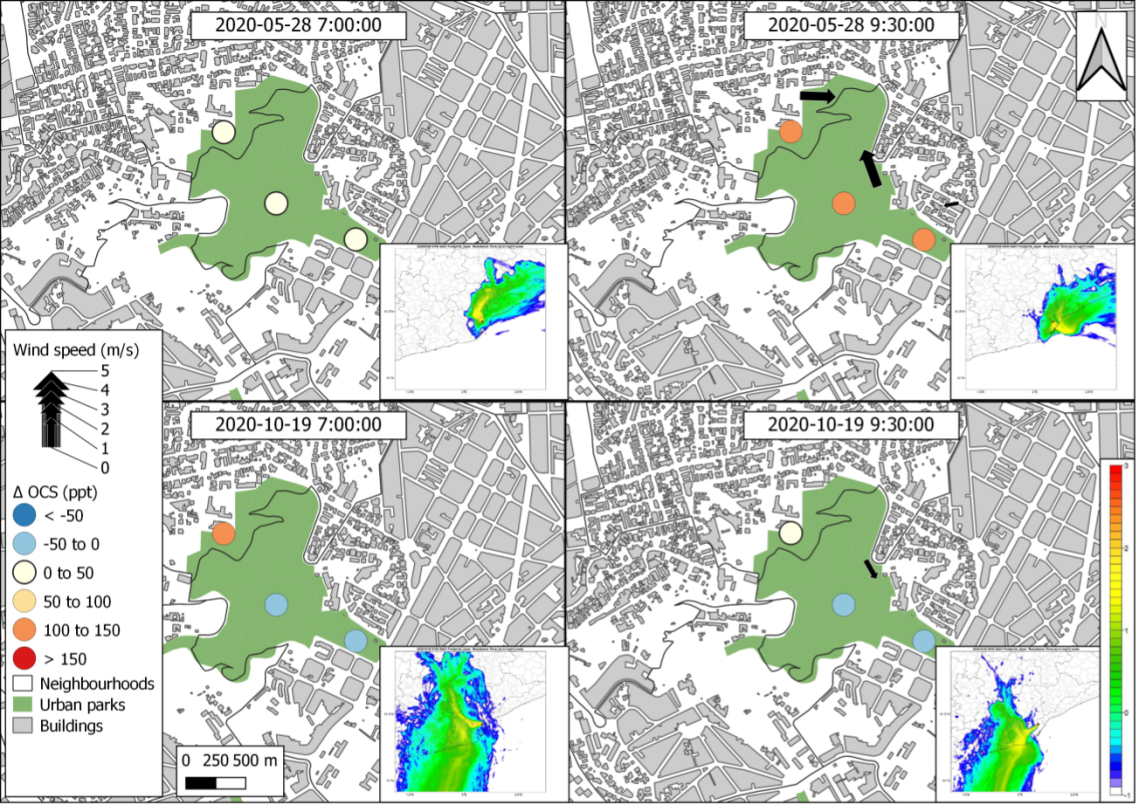


Figure 5b.

2020-05-20 7:00:00

2020-05-20 9:30:00



Wind speed (m/s)

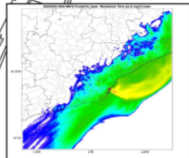
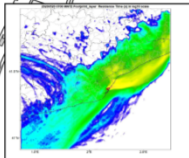
5  
4  
3  
2  
1  
0

$\Delta$  OCS (ppt)

- < -50
- 50 to 0
- 0 to 50
- 50 to 100
- 100 to 150
- > 150

Neighbourhoods  
Urban parks  
Buildings

0 500 1.000 m



2020-10-21 7:00:00

2020-10-21 9:30:00

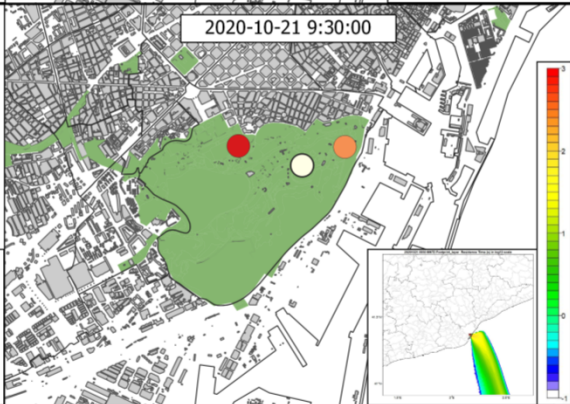
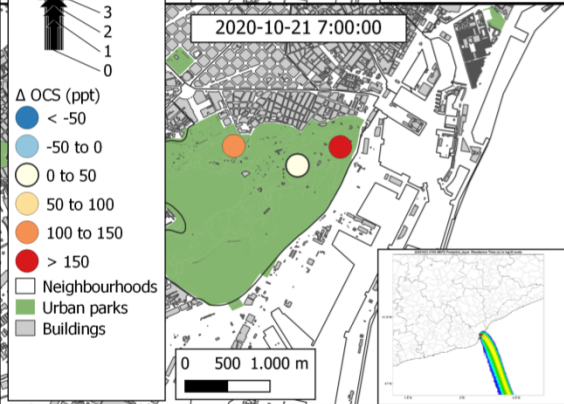
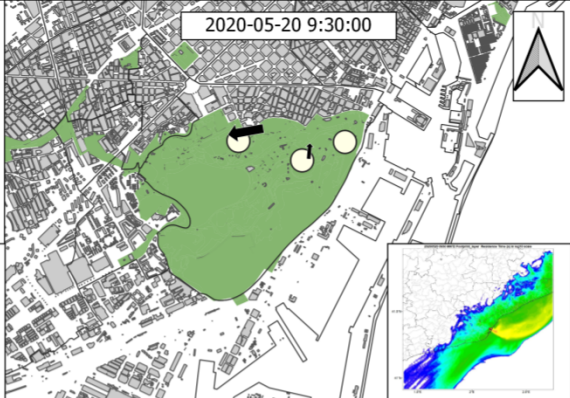
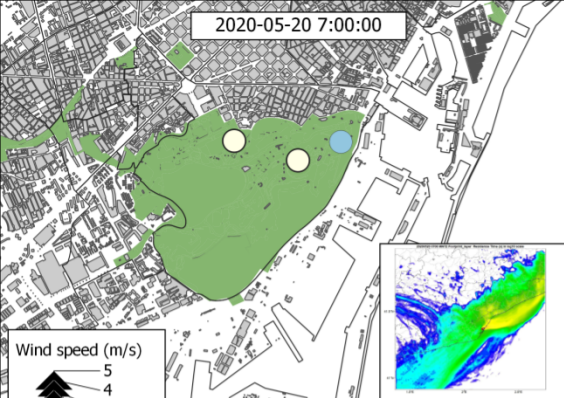
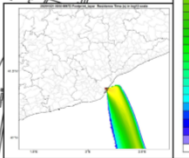
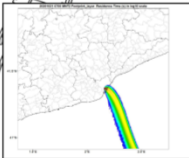
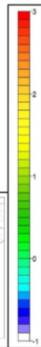
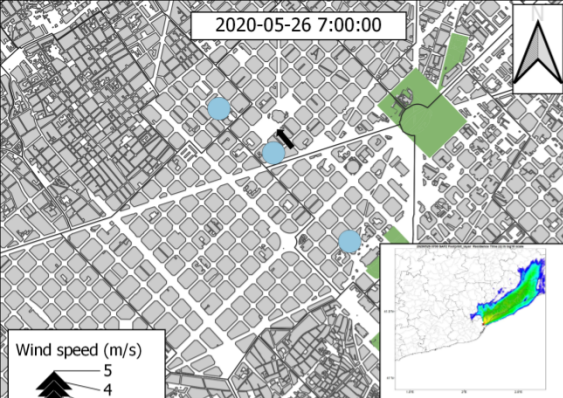


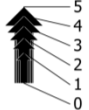
Figure 6a.

2020-05-26 7:00:00



2020-10-20 7:00:00

Wind speed (m/s)

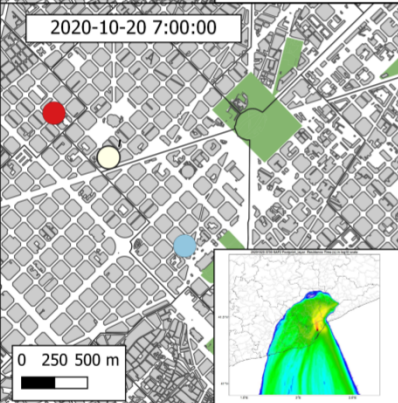


$\Delta$  OCS (ppt)



□ Neighbourhoods  
■ Urban parks  
■ Buildings

0 250 500 m



2020-10-20 9:30:00

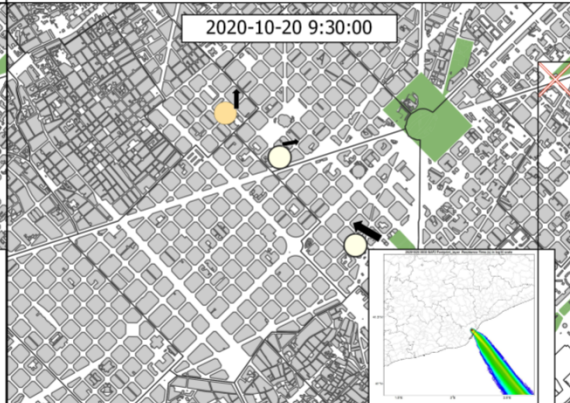


Figure 6b.

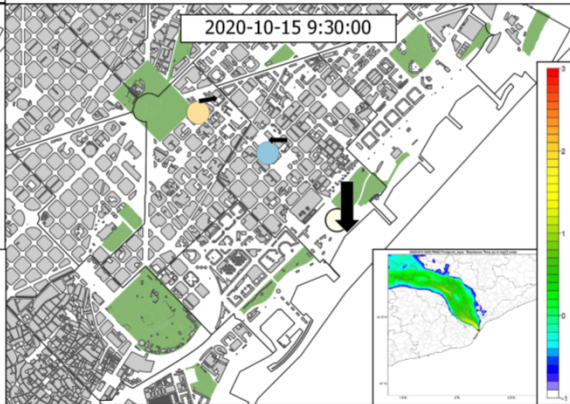
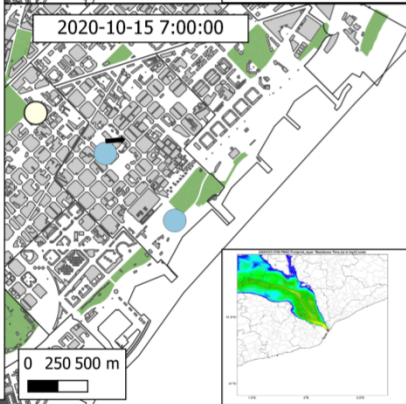
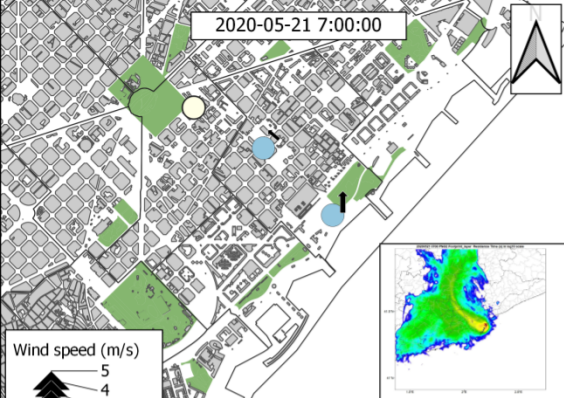


Figure 7a.

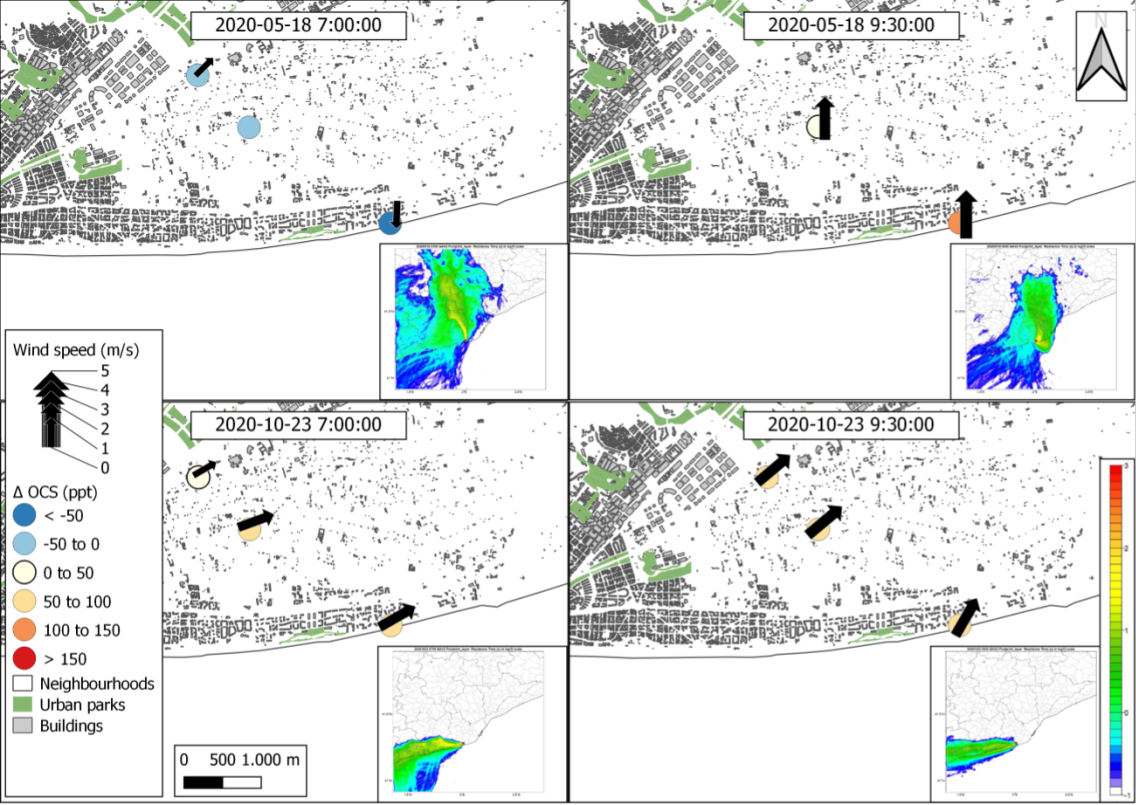


Figure 7b.

